YALE PEABODY MUSEUM

JOURNAL OF MARINE RESEARCH

The *Journal of Marine Research,* one of the oldest journals in American marine science, published important peer-reviewed original research on a broad array of topics in physical, biological, and chemical oceanography vital to the academic oceanographic community in the long and rich tradition of the Sears Foundation for Marine Research at Yale University.

An archive of all issues from 1937 to 2021 (Volume 1–79) are available through EliScholar, a digital platform for scholarly publishing provided by Yale University Library at https://elischolar.library.yale.edu/.

Requests for permission to clear rights for use of this content should be directed to the authors, their estates, or other representatives. The *Journal of Marine Research* has no contact information beyond the affiliations listed in the published articles. We ask that you provide attribution to the *Journal of Marine Research.*

Yale University provides access to these materials for educational and research purposes only. Copyright or other proprietary rights to content contained in this document may be held by individuals or entities other than, or in addition to, Yale University. You are solely responsible for determining the ownership of the copyright, and for obtaining permission for your intended use. Yale University makes no warranty that your distribution, reproduction, or other use of these materials will not infringe the rights of third parties.

The mean circulation of the Atlantic Ocean north of 30S determined with the adjoint method applied to an ocean general circulation model

by Andreas Schiller[1,2]

ABSTRACT

The large-scale mean circulation of the Atlantic Ocean is examined using a general circulation model (GCM) and its approximate adjoint. A cost function is specified that requires the model inputs to be consistent with hydrographic observations and observed air-sea fluxes of heat and freshwater, whereas the velocity field has to adjust to the modified thermohaline initial and boundary conditions.

The optimized, quasi-steady model state is closer to the observed circulation state than previous prognostic steady-state models of comparable resolution. However, it is only partially consistent with the error estimates derived from the observations. In the western boundary region large deviations of the optimized surface fluxes from the observations occur. Additionally, the heat release of the ocean shows unrealistically high values at around 60N. At quasi-equilibrium, in large parts of the thermocline values for temperature and salinity along the Gulf Stream and the North Atlantic current are significantly lower than those in the hydrographic data, thus tending toward winter-time conditions. The model produces a meridional overturning cell with maximum values of 16 to 23 Sv for different experiments. The corresponding heat transports reach maximum values between 0.83 and 1.07×10^5 W.

Model deficiencies like the inappropriate spatial and temporal resolution obviously prevent realistic estimates of water mass distributions and surface fluxes not only in the area of the western boundary current. Another shortcoming of the presented results is the parameterization of eddies and subgrid-scale processes by poorly known diffusion coefficients. To overcome these problems at least partly, future models based on the adjoint method should have a seasonal and increased spatial resolution.

1. Introduction

A major limitation of prognostic GCMs arises from the uncertainties in the atmospheric forcing fields and from the parameterization of subgrid-scale processes. For a long time ocean modellers have been interested in obtaining improved estimates for these model parameters. The efforts, however, were restricted to models with simplified ocean dynamics (e.g., Wunsch, 1978; Hogg, 1987). More

---

1. Institut für Meereskunde, Düsternbrooker Weg 20, 24105 Kiel, Germany.
2. Present address: Max-Planck-Institut für Meteorologie, Bundesstraße 55, 20146 Hamburg, Germany.

recently, complex assimilation schemes became available in oceanography. Especially the adjoint variational method has been used to get improved estimates of ocean circulation parameters. Some of the results obtained so far with the adjoint method are described in Schlitzer (1993), Tziperman *et al.* (1992) and Marotzke and Wunsch (1993). Schlitzer (1993) determined the large-scale mean circulation of the Atlantic, assuming that the velocity is in approximate geostrophic balance with the observed density field. Tziperman *et al.* (1992) used a GCM with simplified momentum dynamics to find a steady state consistent with error estimates for the Levitus (1982) climatology by integrating the model only one forward and the adjoint model only one backward time step. Marotzke and Wunsch (1993) extended the Tziperman *et al.* (1992) approach using a similar model that allowed, however, for much more than just one time step. They tried to find a steady state consistent with error estimates of the North Atlantic hydrography during 1981–1985. Their model produced a final state which was steady within the limits of the estimated observational error. However, the estimated western boundary current thermocline was both colder and fresher than the observations. In addition to the above named models, this paper describes the first attempt using a full primitive equation model and its approximate adjoint to determine the mean circulation of the Atlantic as well as improved estimates for the thermohaline forcing fields of the model.

We represent an attempt to improve some model parameters through application of the adjoint method. The method can generally be understood as a tool for optimally combining data with models, finally producing optimum values for inaccurately known model parameters. The principle advantage of the adjoint method over previously used algorithms lies in its applicability to large systems. The adjoint formalism is particularly appropriate for complex nonlinear and time-dependent systems with a large number of variables. The variables might be initial and boundary conditions, for which optimum values are sought. Additionally, the adjoint method is computationally efficient to determine all gradients of the variables with one backward integration of the adjoint equations (comparable to the corresponding forward model). A subsequent application of an appropriate minimization algorithm yields new estimates for the model variables.

An approximate adjoint to the Bryan-Cox Ocean Model (Bryan, 1969; Cox, 1984) has been constructed which is based on the adjoint equations for the temperature and salinity fields. The main objective is to determine values for the surface fluxes of heat and freshwater which are consistent both with the equilibrium dynamics of the model and with the observed hydrographic data. The task is formulated as an optimization problem, seeking values for the model inputs that minimize a cost function measuring departures from the data and from the steady state. The forward model is the full version of the Bryan-Cox code based on conservation equations for mass, momentum, heat and salt, while the equations constituting the adjoint model are the conservation equations for heat and salt, respectively. A best fit of the model

time trajectory to the data is found through computation of new estimates for the thermohaline forcing and the initial values of temperature and salinity using the adjoint method. Within every forward run, the velocity adjusts geostrophically to new estimates of the thermohaline boundary conditions and initial hydrographic fields.

For the details of our specific adjoint approach we refer the reader to Schiller and Willebrand, 1995 (SW95 hereafter), where we describe our method of obtaining improved model estimates for the hydrography and the air-sea fluxes. Concerning the surface forcing, we simplified the problem and restricted our attention to the fluxes of heat and freshwater, keeping the wind stress field unchanged. The inverse model was tested using a basin-scale model with simulated data (identical twin experiments), where the true solution of the optimization problem is precisely known. The result suggests that one can expect improved estimates for the thermohaline surface fluxes and the hydrography when using real instead of simulated oceanographic data. However, it became obvious throughout the experiments that in regions with strong convective activity the inverse model is not able to produce satisfactory results. This is presumably due to the strong nonlinear character of the convective adjustment processes.

Combining a complex numerical model of the ocean circulation with different data sets and with a minimization algorithm poses a lot of practical problems. Because this part of oceanography is still at its beginning, we will keep the technical expenditure (e.g. the way of interpolating model values to data points) as small as possible. The simplifications will be discussed in detail, and it is suggested to improve them in future experiments with similar optimization methods.

As a first step toward a more realistic description of the ocean's state by GCMs the "steady state" or "mean" circulation is investigated. Although this concept does not take into account important aspects of variability in the real ocean circulation, it has nevertheless widely been used by the oceanographic community to compare model results with temporally averaged distributions of observed water mass properties.

The main objectives of the present paper can be formulated as follows:

• Are the hydrographic observations consistent with the observations for the surface fluxes of heat and freshwater?

• Using these observations, does the final model state describe a steady circulation of the Atlantic Ocean with plausible mean distributions of water mass properties?

The answers to these questions are strongly related to the quality of the observations and the validity of the model. While for the observations error estimates allow to weight the confidence one has into the data, the errors in the model and its equations are not considered by the adjoint formalism. We will demonstrate in the next sections that the failure of the model to describe the observed properties of the
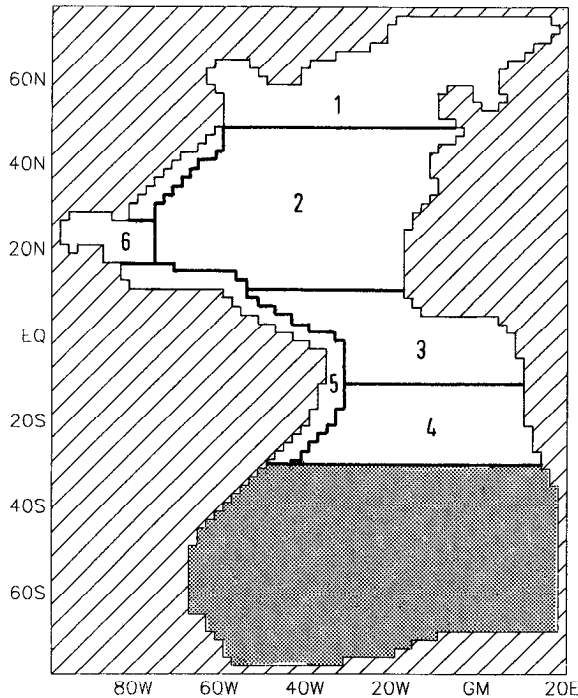
Figure 1. Model area. Shaded: Southern model area where no optimization is performed but with restoring the hydrography to Levitus data. Numbers denote areas where individual error estimates were computed for the hydrographic data (experiments S1–S3): (1) Subpolar region, (2) Subtropical Atlantic, (3) Equatorial Atlantic, (4) Subtropical South Atlantic, (5) Western boundary currents, (6) Caribbean Sea/Gulf of Mexico.

ocean circulation in a realistic way crucially influences the results of the inverse model.

In Section 2, we describe some details of the Atlantic model and the data base used for assimilation. The performance of the pure prognostic model using different surface boundary conditions is demonstrated in Section 3. Results of the inverse model are presented in Section 4, followed by a discussion in Section 5.

2. Experimental strategy

a. Model description. The physics of the GFDL Ocean Model (Bryan, 1969; Cox, 1984) and its adjoint was described in SW95. The Atlantic model is configured with realistic topography, extending from 77S to 75N and from 97W to 19E (Fig. 1). The horizontal resolution is 2° in both dimensions, with 12 levels in the vertical. Level spacing and depths are equal to the configuration used by Gerdes *et al.* (1991).

In our experiments we will concentrate on the thermohaline circulation north of 30S. This restriction is motivated by the reduced hydrographic data base available in

the South Atlantic. The large-scale circulation in the North Atlantic, however, is strongly influenced by the South Atlantic, in particular through the Antarctic Intermediate Water (AAIW) and the Antarctic Bottom Water (AABW). We did take into account these influences by restoring the temperature and salinity fields to the climatology of Levitus (1982) south of 30S. This was done with a depth-dependent time constant varying between 30 and 250 days from the surface to the bottom layers.

The southern buffer zone affects the results of the optimization too. Although the Levitus climatology is locally incorrect, it nevertheless reproduces the large-scale features of the circulation. In preliminary experiments without any restoring to the Levitus data in the South Atlantic the optimization north of 30S produced stronger deviations from the hydrography than with sponge layers south of it.

The Arctic and the Mediterranean Seas are significant for determining the overall density structure of the North Atlantic. In order to limit the complexity of our model we simplified the boundary conditions, however, accepting worse results in those areas of the model which are directly influenced by these marginal seas. We assumed a negligible transport across 75N, i.e. the northern boundary is closed without any restoring zone. A Mediterranean Sea is not included in the model configuration.

In the northern part of the model area the thermohaline surface fluxes have been formulated as flux conditions, whereas in the southern part of the model domain a Newtonian damping law with a time constant of 30 days is used to adjust the sea surface temperatures and salinities to the Levitus data (Haney, 1971).

Annual mean values for the wind stress field are taken from Hellerman and Rosenstein (1983). As already explained in SW95, the wind stress is not optimized in the procedure applied here. In our subsection about the mean circulation we will draw some conclusions from sensitivity experiments we performed with different wind fields.

We have not attempted to include inaccurately known diffusion coefficients into the optimization formalism. Instead we have investigated the sensitivity to different diffusion parameters. The diffusion terms in the conservation equations for heat and salinity parameterize processes that cannot be resolved by the model grid, such as mesoscale geostrophic eddies and small scale turbulence through internal waves. For the lateral diffusion we have used an isopycnal diffusion scheme in two experiments, as formulated by Redi (1982), Cox (1987) and Gerdes (1988). The isopycnal diffusion coefficient was allowed to vary exponentially from top $(1.0 \cdot 10^3$ m^2/s) to bottom $(3.0 \cdot 10^2$ m^2/s). To suppress effects of numerical dispersion resulting from the central difference advection scheme, a certain amount of explicit diffusion in the direction of coordinates is necessary $(3.0 \cdot 10^2$ m^2/s). It was noticed by Gerdes *et al.* (1991) that along the lateral model boundary negative diffusion, resulting from the discrete structure of the model, has to be suppressed by introducing boundary layers

with the distance of one grid point. Along these boundaries a cartesian instead of an isopycnal diffusion is used ($3.0 \cdot 10^2$ m^2/s).

The vertical mixing of ocean water mass properties in GCMs is usually described by a Fickian diffusion law, parameterizing processes such as small scale three-dimensional turbulence, double diffusion and effects of the nonlinear equation of state. On an ocean scale, little is known about the spatial structure of these processes. For this reason modellers mainly used a constant value for the vertical diffusivity. Based upon a review of estimates of the vertical diffusion coefficient from observations, Gargett (1984) proposed to use a stability-dependent parameterization for the vertical diffusivity. This approach was explored in GCMs by Cummins *et al.* (1990) and Gargett and Holloway (1992). The vertical diffusion coefficient is assumed to be proportional to the local Brunt-Väisälä frequency N, i.e. it is dependent on the stratification and on internal waves:

$$
K_v = \begin{cases} a_0 \cdot N^{-1} \dfrac{\text{m}^2}{\text{s}} : & \dfrac{\partial \rho}{\partial z} < 0 \\[2mm] 1.0 \dfrac{\text{m}^2}{\text{s}} : & \dfrac{\partial \rho}{\partial z} \geq 0 \end{cases} \tag{1}
$$

with

$$
a_0 = 10^{-7} \frac{\text{m}^2}{\text{s}^2} .
$$

The value of 1.0 m^2/s characterizes strong mixing in case of static instability. We will combine this approach (Eq. 1) with the isopycnal diffusion tensor and in two additional experiments with a cartesian diffusion ($K_h = 1.0 \cdot 10^3$ m^2/s). To complete the set of different diffusion parameterizations, constant diffusion coefficients will be used in a third model configuration ($K_h = 1.0 \cdot 10^3$ m^2/s, $K_v = 1.0 \cdot 10^{-4}$ m^2/s).

b. Data base. To provide data for the annual mean values of surface heat flux and evaporation the observations from the "Comprehensive Ocean Atmosphere Data Set" (COADS, Woodruff *et al.*, 1987) have been used. The surface fluxes were calculated by using revised Bunker wind fields and bulk coefficients (Isemer and Hasse, 1991; Isemer, personal communication, 1992). Figure 2 shows the observed annual mean value of the surface heat flux interpolated onto the model grid. Large parts of the model area are characterized by a heat release of the ocean to the atmosphere with maximum values along the western boundary current (-225 W/m^2). Heat uptake of the ocean is dominant in the upwelling regions off the African coast, in the equatorial region and off the Newfoundland coast.

The flux of freshwater across the ocean-atmosphere interface is defined as the difference of precipitation minus evaporation. The evaporation values from the
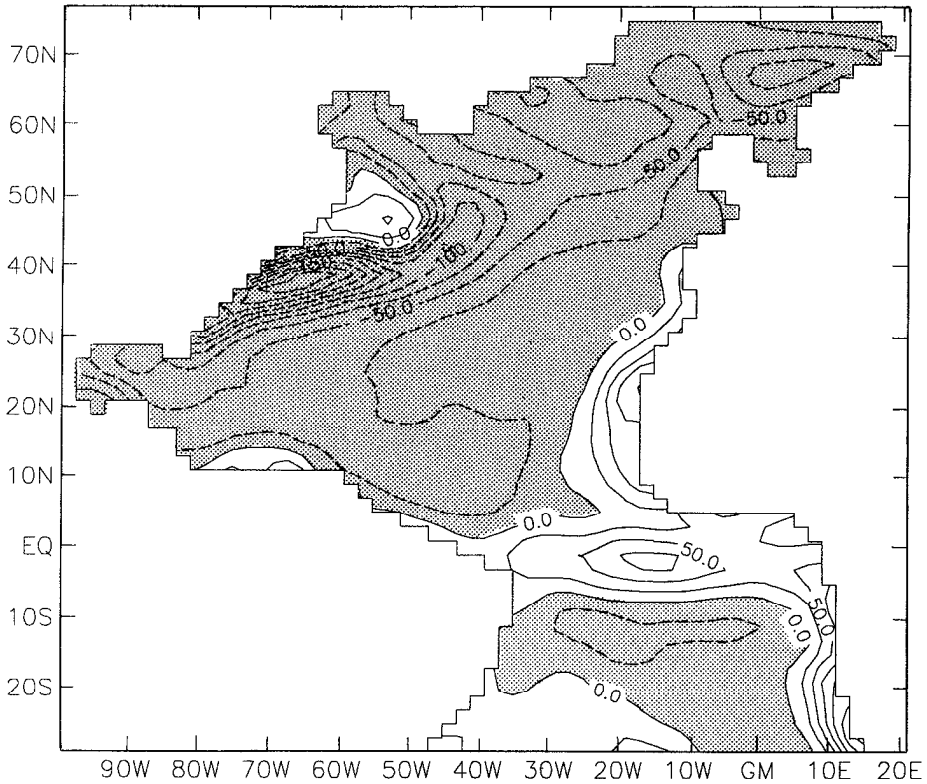
Figure 2. Annual mean surface heat flux based on COADS data (Woodruff *et al.*, 1987), negative areas are shaded. C.I. = 25.0 W/m². (Positive values denote heat gain of the ocean.)

COADS data have been combined with the precipitation values of Dorman and Bourke (1981). Both data sets have been interpolated onto the model grid and the observed freshwater flux is shown in Figure 3. In the subpolar area and the equatorial intertropical convergence zone the annual mean of precipitation exceeds that of evaporation. Evaporation is dominant in the subtropics of both hemispheres with minimum values for the freshwater flux along the Gulf Stream (< −2.0 m/y).

The hydrographic observations consist of two different data sets. The first one was the atlas from Levitus (1982). The second data base was obtained by merging all the station data sets and individual ship cruises that had been available to us. It is known that the Levitus data reflect the large-scale structures of ocean property distributions, but they are smoothed in regions of strong gradients, especially along the western boundary currents (Olbers *et al.*, 1985). Our hydrographic data set contains about 5700 historic and recent bottle casts and CTD measurements which have been interpolated to standard depths. The overall data coverage is shown in Figure 4. A complete listing of the origin of the data can be found in Schiller (1993). In the polar
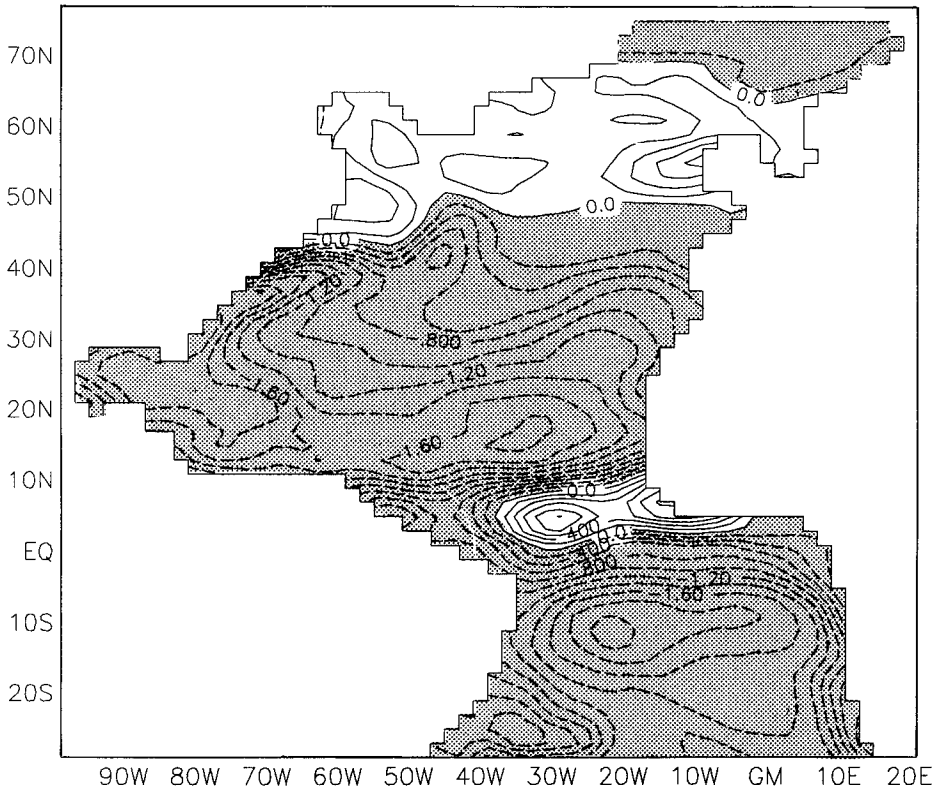
Figure 3. Annual mean freshwater flux (precipitation minus evaporation) based on COADS
data (Woodruff *et al.,* 1987) and on data from Dorman and Bourke (1981), negative areas
are shaded. C.I. = 0.2 m/y.

area, in the central North Atlantic and in the South Atlantic the data coverage
remains rather poor.

The model to data comparison in the cost function was handled as follows.
Although, in principle, it would be possible to interpolate the model variables from
grid points to the respective observations, this procedure would require an interpola-
tion of the model variables to the coordinates of the observations for every computa-
tion of the cost function. Instead of implementing such a technical complex task, we
interpolated the hydrographic data to the model grid points before starting the
optimization procedure. All temperature and salinity data within a model box have
been interpolated with equal weights to the appropriate tracer point at the center of
the box. The resulting geographical error due to this averaging procedure is about
1.4° at most, which is less than the averaging scale that has been determined for the
Levitus data (Olbers *et al.,* 1985). One has to keep in mind, however, that averaging
on z-levels may cause anomalous water mass characteristics. This has been pointed
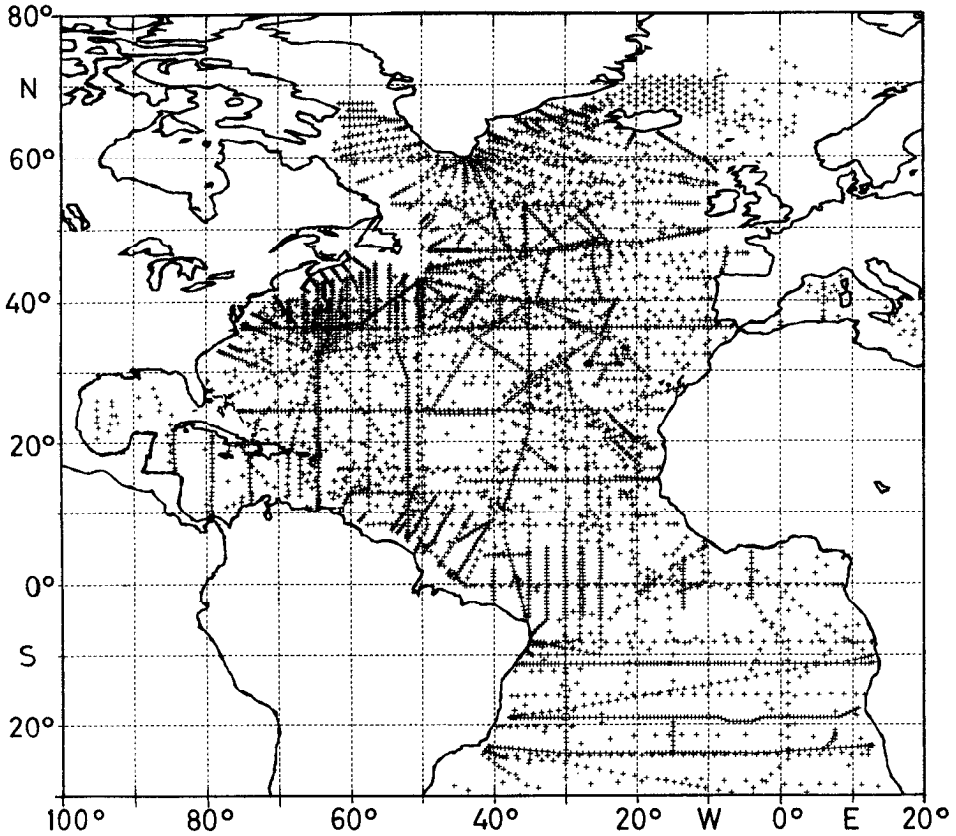out recently in the Atlantic climatology constructed by Lozier *et al.* (1994), whereas

Figure 4. Spatial distribution of hydrographic station data used in this study.

averaging on isopycnal surfaces maintains the local water mass properties. Especially along sharp frontal regions such as the Gulf Stream and the North Atlantic Current the comparison of the averaged results showed striking differences.

Using hydrographic data in a model with stationary forcing may cause problems because of the temporal and spatial variability in the data. Especially the effects of mesoscale eddies and seasonal effects on temperature and salinity cannot be reproduced by the model and have to be taken into account in the error estimates of the cost function. We will discuss this point in more detail in the next subsection.

c. Experimental procedure. All experiments have been started from the observed distributions of temperature and salinity. In the case of hydrographic station data, after interpolating them to the model grid about 81% of the model grid points were covered by the observations. At the remaining grid points the Levitus data have been used to complete the first guess fields. In this case, however, the cost function

Table 1. Classification of experiments. Cart.: Diffusion along the direction of coordinates, otherwise along isopycnals. Diffusion in L1, L3, S1 and S3 is vertically variable, depending on the stability frequency N.

Experiment	L1	L2	L3	S1	S2	S3
Observations of surface fluxes		Heat flux and evaporation: COADS data (Woodruff *et al.,* 1987), Precipitation: Dorman & Bourke (1981)				
Hydrographic observations		Annual mean values from Levitus atlas (1982)			Hydrographic station data	
Parameterization of diffusion	cart. vert. $K_v(N)$	cart. constant	isopycnal vert. $K_v(N)$	cart. vert. $K_v(N)$	cart. constant	isopycnal vert. $K_v(N)$

contains only the data − model differences between the hydrographic data and the model values.

The first guess fields for the velocity were taken from spin-up runs of a purely prognostic model, started from the Levitus climatology. This procedure guarantees that the initial model velocities are not too far away from a large-scale geostrophic velocity field. In addition, numerical problems that might arise when starting a model from a zero velocity are avoided.

The experiments can be classified by the kind of diffusion and the kind of hydrographic data used. Instead of discussing all experiments in full detail, we will focus our attention on the question of reproducibility of the observed fields by the model within the observation errors. In addition to the general questions posed in the introduction, we will investigate whether the isopycnal diffusion gives the most reasonable results in the context of our inverse approach. Finally, we will explore the performance of the inverse model when using different hydrographic data sets and simultaneously optimizing the thermohaline surface fluxes. Six different experiments are presented in this paper. Their arrangement is shown in Table 1.

In accordance with the results of our identical twin experiments (SW95) we chose an integration time of one year at the beginning of the minimization procedure. Within this short integration time a mutual adjustment of the near-surface hydrography and the thermohaline forcing takes place. As the iterations become less efficient in reducing the cost function (i.e. less than one percent reduction in two successive iterations), the minimization procedure is restarted with an increased integration time of five years. The restart uses the final, rather than the initial state of the previous minimization as first guess. Increasing the integration time in combination with the restart allows the model hydrography of the deeper ocean to begin to adjust to the surface forcing. If the reduction of the cost function becomes less efficient even for the five year integration period, the minimization procedure is restarted with the final values of the previous optimization until no further reduction in the cost function is obtained. In this way, a total integration time of 10 to 20 years is obtained,

depending on the number of restarts. This integration time is similar to the time scale that was identified by Sarmiento and Bryan (1982) and Cox and Bryan (1984) for the ventilation of the thermocline in the subtropical gyre in numerical circulation models.

Another positive effect of the increased integration time is the disappearance of strong meridional overturning cells near the equator. The unrealistic phenomenon encountered in primitive equation models has its origin in the "bottom torque"-term of the barotropic vorticity equation (Sarmiento and Bryan, 1982). It is caused by an incompatibility of the observed, but smoothed large-scale density field with the smaller-scale bottom topography. The effect disappears after a few years of integration time, since the temporal evolution of the density field in the model allows compensation for this effect.

Missing information on the observation errors in data sets poses a frequent problem to inverse modellers (e.g. Olbers *et al.,* 1985; Hogg, 1987). The Levitus atlas (1982) contains oceanwide averaged standard errors for the Atlantic that we used as observation errors for the Levitus data. The observation errors range from 1.4°C and 0.28 psu at the surface down to 0.3°C and 0.02 psu near the bottom for temperature and salinity, respectively. For the averaged hydrographic station data we tried to obtain regional error estimates. To this purpose the standard errors were computed when the station data were interpolated onto the model grid. Subsequently, these standard errors have been averaged for the six model areas denoted in Figure 1. The errors computed for the station data are always smaller than the Levitus error estimates. We chose values of 0.01°C and 0.01 psu for temperature and salinity, respectively, as lower error limits. Smaller errors would be inconsistent with generally accepted assumptions about errors in climatological data sets (Olbers *et al.,* 1985).

In our first study (SW95) we described the coupling between observation error and the demand for a steady state. The same procedure was also applied to the present problem. Based on observations, Levitus (1989) discussed a temporal variability of the large-scale ocean circulation with a time scale of about 20 years. In approximate accordance with his results, we allowed the temporal changes in temperature and salinity extrapolated over 20 years to have the same magnitude as one standard deviation between model and observation.

No direct error estimates were available for the surface flux data. We have taken 25 W/m^2 for the error of the surface heat flux which is comparable to the heat flux error of Isemer *et al.* (1989). The error for the freshwater flux has been set somewhat arbitrarily to 0.5 m/y.

3. Preliminary experiments with the prognostic model

In this section we will demonstrate the necessity to optimize the thermohaline surface fluxes in the context of a numerical ocean circulation model. Two experi-

ments have been performed, both using a cartesian diffusion with a stability dependent vertical mixing. Both experiments were started from the Levitus climatology, but they differ in the formulation of the thermohaline forcing. In the first experiment a standard Newtonian boundary condition with a time scale of 30 days has been employed. Starting from the Levitus climatology, the model was integrated for 500 years so that the upper layers (though not the deep ocean) were in near-equilibrium. Figure 5a shows the diagnosed surface heat flux after 500 years of integration time. The surface heat flux qualitatively reproduces some large-scale features of the observed surface heat flux (cf. Fig. 2), such as a strong heat release in the western boundary current region and the heat uptake at the equatorial zone. Locally, however, significant differences to the observations become obvious. Along the western boundary current the heat release of the model is restricted to a small area along the American coast. In the observations this area extends further offshore. The strong heat uptake south of Greenland is not consistent with observations and has its origin in too strong advection of cold surface water masses southeastward with the Labrador Current. Due to the coupling between surface temperatures and prescribed climatological values, a strong heat uptake is produced in this model area. The heat release along the northern boundary can be traced back to the northward transport of warm water masses with the North Atlantic Current (NAC) and the Norwegian Current. Similar results are obtained for the freshwater fluxes with large deviations from the observations (not shown). Especially in the Gulf Stream region and north of 60N the freshwater fluxes seem to be unrealistic. Figure 5b shows a section along 31W for potential temperature. It is important to note that in contrast to the surface fluxes the model hydrography remains almost identical to the observed distributions, because the surface temperatures (and salinities) are effectively set to the prescribed climatology. The meridional overturning is weak with several cells of about 5 Sv (not shown).

   In the second experiment (configuration L1 in Table 1) we implemented the thermohaline boundary conditions as flux boundary conditions that were constant in time with the observed distributions for heat and freshwater fluxes shown in Figure 2 and 3. The model was integrated again for 500 years. The temporal evolution of the model state was somewhat unexpected. The model ocean loses heat over large parts due to an area averaged heat release in the heat flux observations of about -19 W/m^2 north of 30S (observed area averaged freshwater flux: -0.87 m/y). The heat uptake near the equator, off the African coast, along Newfoundland and at the South American coast is unable to stop this cooling trend. At the beginning of the integration the northward heat transport out of the restoring zone south of 30S is too weak to compensate for the surface heat release. After 25 years, however, a strong meridional overturning cell has developed, that has its maximum at 17N and for a time reaches more than 100 Sv (Fig. 6a). The model tries to compensate for the strong heat release through the surface by a strong northward transport of heat out
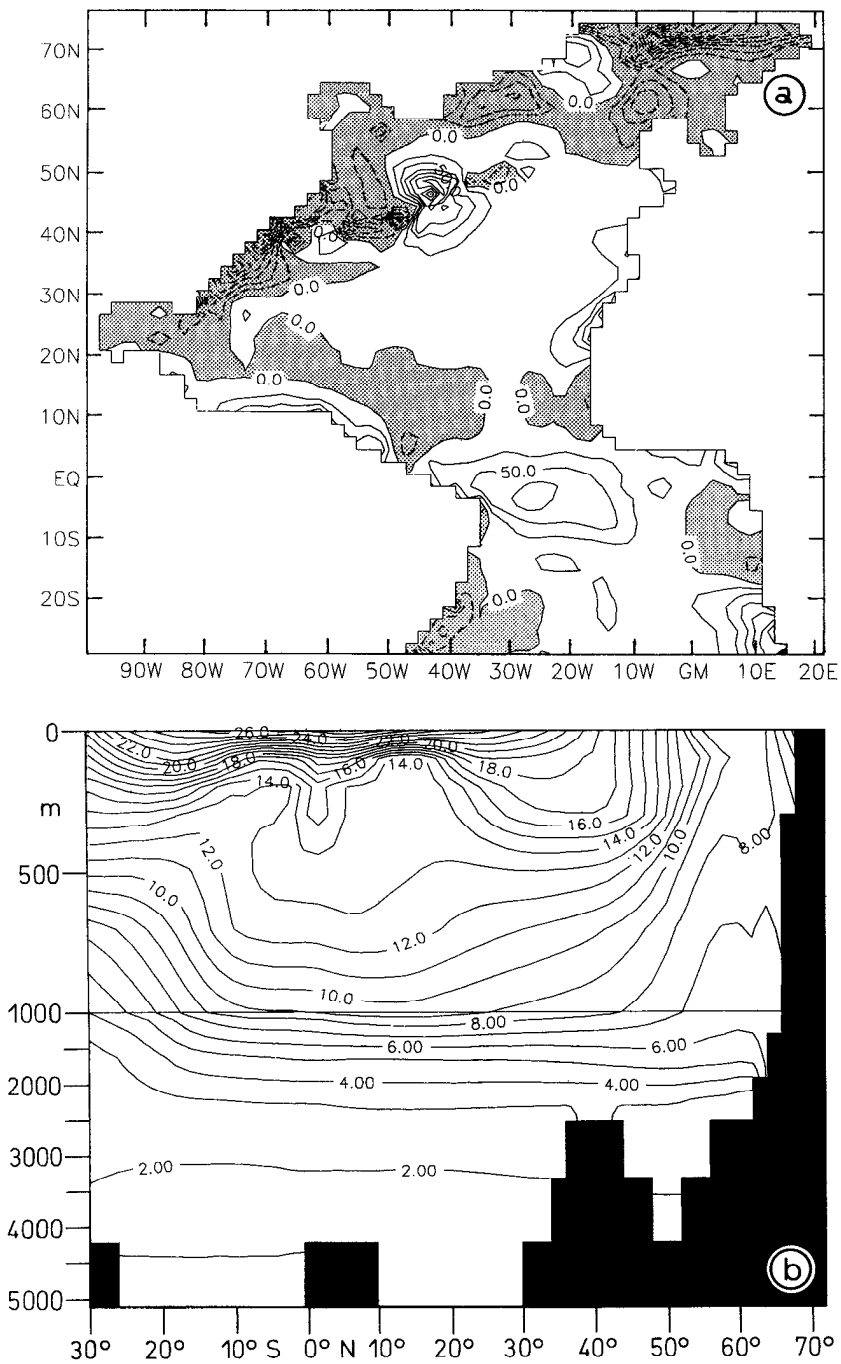
Figure 5. Prognostic model with Newtonian boundary condition. (a) Surface heat flux after 500 years of integration time, negative areas are shaded. C.I. = 25.0 W/m². (b) Potential temperature along 31W after 500 years of integration time, C.I. = 1.0 °C.
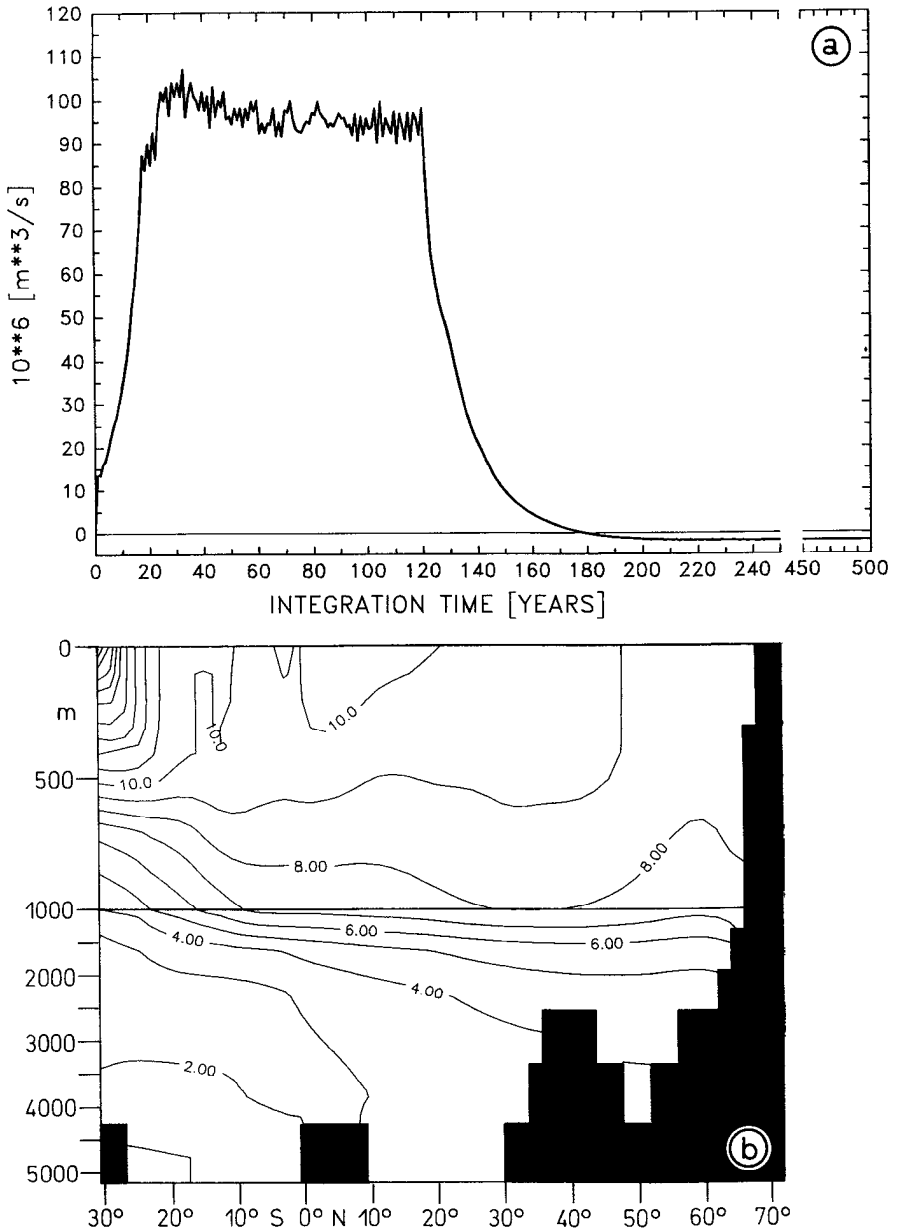
Figure 6. Prognostic model with fixed flux boundary conditions. (a) Time series of zonally integrated volume transport at 17N (maximum value). (b) Potential temperature along 31W after 500 years of integration time, C.I. = 1.0 °C.

of the southern buffer region (about 1.2×10^{15} W caused by strong meridional overturning). This phenomenon can be pursued up to an integration time of about 120 years. Subsequently, the meridional overturning breaks down on a time scale of approximately 30 years. Only the Ekman component is maintained in the following period, no further drastic changes in the model state have been observed. However, even after 500 years of integration no steady state is achieved. The northward heat transport across the southern buffer zone is almost zero and therefore does not contribute to the heat budget of the model volume north of 30S. The area averaged heat loss through the surface of -19 W/m^2 causes a continous cooling trend in the northern model volume. The potential temperature along 31W after 500 years of integration time is shown in Figure 6b. Outside the area of influence of the southern boundary the hydrography shows large deviations from the observations and' is characterized by small spatial gradients.

To summarize the results of both experiments, one obtains an unsteady model state with strong deviations of the model hydrography from the observations when using observed surface fluxes as flux boundary conditions. On the other hand, using a Newtonian boundary condition, the results exemplify that the hydrography is close to the observations, but the surface fluxes are rather unrealistic. As a consequence of both experiments presented here, it is evident that an optimal and more realistic model state can be obtained only by simultaneously varying the hydrography and the surface fluxes. This attempt will be investigated in the next sections through applying the adjoint approach to the model, to the hydrographic data and to the surface flux data together.

4. Results of the inverse model

In this section we will concentrate on the data—model comparison. It is not intended to give a complete documentation of all results. Instead, we try to give an idea of the general difficulties of the inverse approach and the differences between the experiments. Hence, we will show and discuss only the most appropriate results for the respective optimized model parameters.

In preliminary assimilation experiments, considerable deviations of the optimized surface fluxes from the observations have been encountered in some parts of the model domain. These deviations were concentrated around 60N, the northern model boundary and along the North American coast. The maximum differences to the data were 550 W/m^2 and 750 W/m^2, respectively. Especially in the northern areas, the unrealistically strong heat release of the ocean could not always be compensated by a realistic magnitude of advection of warmer water masses. Thus, at some grid points the freezing temperature was reached. The strong heat release along the Gulf Stream is related to the well-known deficit of primitive equation models, in which the Gulf Stream separates too far to the north from the American coast (Sarmiento, 1986; Treguier, 1992). Consequently, along the American coast and north of about

35N the model temperatures are too high compared to observations. To keep the model surface hydrography close to the observations a strong heat release from the ocean is necessary. Similar problems have been encountered for the freshwater fluxes along the North American coast. In the model the Gulf Stream transports saline water too far northward, whereas in reality at the same locations the Labrador Current advects less saline water to the south. Consequently, the model tries to reduce this discrepancy by a huge freshwater flux of 15 m/y.

Neither the enormous heat releases in the northern model area and along the American coast nor the strong precipitation excess in the Gulf Stream area are consistent with observations. As a consequence, we decided to introduce a flux limitation for the surface fluxes. This limitation allows the optimized surface fluxes to deviate locally by no more than three times from their estimated errors, i.e. 75 W/m^2 and 1.5 m/y at maximum, respectively. It will be demonstrated in the subsequent experiments that these restrictions are important mainly in the above mentioned problem regions, while for the majority of the model area the data—model differences are within the maximum limits.

It was noticed by one of the referees that 75 W/m^2 as a limit on deviations of the estimated surface heat fluxes from the climatology is very low. Isemer *et al.* (1989) give errors between 20 and 40 W/m^2 for the uncertainties in the coefficients that have been used to compute the fluxes. The error estimates of Isemer *et al.*, however, do not include errors from sea surface temperature and air temperature. As a consequence, the heat flux limitation of 75 W/m^2 as it is used in the experiments below is rather a lower bound.

a. Analysis of the cost function. All experiments have been carried out following the concept as described in Section 2. The number of iterations varied between 28 (exp. S3) and 53 (exp. L1). Table 2 shows the total and individual cost function values of the experiments. One task of the applied inverse mechanism is to find a compromise between the requirement for a steady model solution and the deviations of the model from the observations. This demand is accomplished by the model, because the steady state residuals in Table 2 have the same order of magnitude as the data— model contributions.

In the case of a perfect model, accurate error estimates would cause all final cost function contributions to equal one standard deviation, documenting that the individual cost function components correspond to just one standard deviation of the *a priori* error estimates. It is a general result of all experiments that no final cost function value J_{end} is smaller or equal unity. Even the experiment with the overall smallest cost function value (L2) exhibits locally strong deviations from the observed hydrography. Note that the experiments with Levitus data show smaller total cost function contributions than the experiments with the smoothed hydrographic station data. The main reason may be found in the generally larger cost function terms of the

Table 2. Cost function contributions. T_{obs}, S_{obs}, $H_{T,obs}$, $H_{S,obs}$ are the (respective) observation terms and ΔT, ΔS are the (respective) steadiness terms in the cost function as described in Schiller and Willebrand (1995). The individual cost function values are normalized by the *a priori* standard errors and by the number of observations (T_{obs}, S_{obs}, $H_{T,obs}$, $H_{S,obs}$) or model grid points (ΔT, ΔS). A unit value equals a global deviation of one standard error of the respective variable from the observations. J_{begin} and J_{end} denote the mean values of the individual cost function contributions at the beginning and at the end of the minimization procedure.

Experiment	Total cost function		Individual contributions to cost function J_{end}					
	J_{begin}	J_{end}	T_{obs}	S_{obs}	ΔT	ΔS	$H_{T,obs}$	$H_{S,obs}$
L1	6.18	1.61	1.91	1.79	1.21	1.12	1.83	1.81
L2	6.77	1.24	1.60	1.54	0.97	0.77	2.01	1.73
L3	6.38	1.67	1.93	1.63	1.63	1.41	1.67	1.80
S1	9.23	3.69	6.14	6.93	2.80	2.06	2.03	2.16
S2	10.06	3.33	5.80	6.14	2.33	1.41	2.25	2.05
S3	9.54	3.27	5.70	5.35	2.30	1.96	2.11	2.22

hydrographic data. The maximum values are 6.93 and 1.93 for hydrographic and Levitus data, respectively. Remembering that the error estimates for the station data are much smaller than those for the Levitus data, it can be seen from Table 2 that the model results deviate stronger from the *a priori* error estimates of the station data than from Levitus' error estimates. Probably one important reason for these differences in the data sets is due to the eddy fields that are still contained in the hydrographic station data, even after the smoothing operation. As a consequence, the observed fields show a noisy structure that cannot be reproduced by the model. Another difference concerns the steady state terms of the cost function. In the Levitus climatology the seasonal components of the temperature and salinity signals are filtered out at least approximately, whereas the hydrographic station data contain a distinct seasonal signal. Keeping the model hydrography close to the hydrographic station data from several seasons produces pronounced temporal changes during the forward integration of the model. The larger temporal changes of the experiments S1-S3 are visible in the steady state contributions to the cost function with the station data values being about twice as large as the respective values for the Levitus data (although the weights have been chosen to be equal). The contributions of the surface flux terms to the cost function in Table 2 are about two standard deviations. Because of the flux limitations, the differences between the individual experiments are rather small. Looking at the cost function values, one has to conclude from the results that the model physics is not compatible with either of the data sets.

b. Local minima. To get an idea about the possible reasons for the inconsistencies between model and data a particular experiment (S1) was repeated. Noise has been added to the first guess with an amplitude of one standard deviation. The final model

state shows an increase of only 3.5% in the total cost function value compared to the model state that was obtained without any noise added to the first guess. Although the results suggest that indeed a minimum of the cost function has been found with the original experiment, we will try rather to identify how the different portions of the cost function influence each other. Changing the hydrography, how does this influence the cost function contributions of the surface fluxes and vice versa? Does bad conditioning prevent a further reduction of the cost function value? To get an answer to these questions, a new cost function has been computed, where the solution vector $\mathbf{X}$ was defined as a linear combination of the two old solution vectors $\mathbf{X}_{min1}$ and $\mathbf{X}_{min2}$ (Tziperman *et al.*, 1992):

$$\mathbf{X}_i = \mathbf{X}_{min1} + \alpha_i \cdot (\mathbf{X}_{min2} - \mathbf{X}_{min1}), \quad \text{with } \alpha = -3.0, -2.8, \ldots, 2.8, 3.0. \quad (2)$$

It is evident from Figure 7 that both solutions $\mathbf{X}_{min1}$, $\mathbf{X}_{min2}$ lie in a flat valley of the parameter space spanned by the solution vector $\mathbf{X}$ (section A). In the valley the model cannot resolve linear combinations of the parameters. Thus, all solutions are acceptable by the minimization. The flatness of the cost surface prevents a further convergence toward a possibly existing smaller minimum. Where does this flat minimum of the cost function come from? The parameter space of the solution vector $\mathbf{X}$ in Figure 7a contains two subspaces, one including the hydrography (T, S) and the other one including the surface fluxes (H_T, H_S). Section B in Figure 7a–e represents the cost function values of the surface fluxes for the solution vector $\mathbf{X}_{min1}$, and the values for the hydrography have been determined according to Eq. 2. Conversely, in section C the hydrography equals the solution vector $\mathbf{X}_{min1}$, and the surface fluxes have been determined according to Eq. 2. The curves of section C are parallel to the curves of section A over a wide range of the shown parameter space (in Fig. 7c the curves are indistinguishable). Keeping the hydrography fixed at the first solution thus influences the cost function of the surface fluxes only marginally. In contrast, section B shows distinct differences to sections A and C. With constant surface fluxes the cost surface flattens in Figure 7b. The data—model difference for section B that is shown in Figure 7d does not have a minimum of the cost function. This seems to indicate that mainly the optimized surface fluxes prevent a further progress in reducing the cost function value. Although the surface fluxes contribute only about one percent to the total cost function values, as model boundary conditions they have an important impact on the cost function values of the hydrography. Finally, we can state that the incompatibility of surface fluxes and hydrography with the model is a main reason for the failure of the minimization algorithm to further reduce the cost function value.

Furthermore, the problem of bad conditioning can be seen in the flatness of the cost surface in Figure 7b. An insensitivity of the cost function in one direction of the parameter space implies that the respective model parameters are not resolved, i.e. they can be represented by linear combinations of other model parameters. The
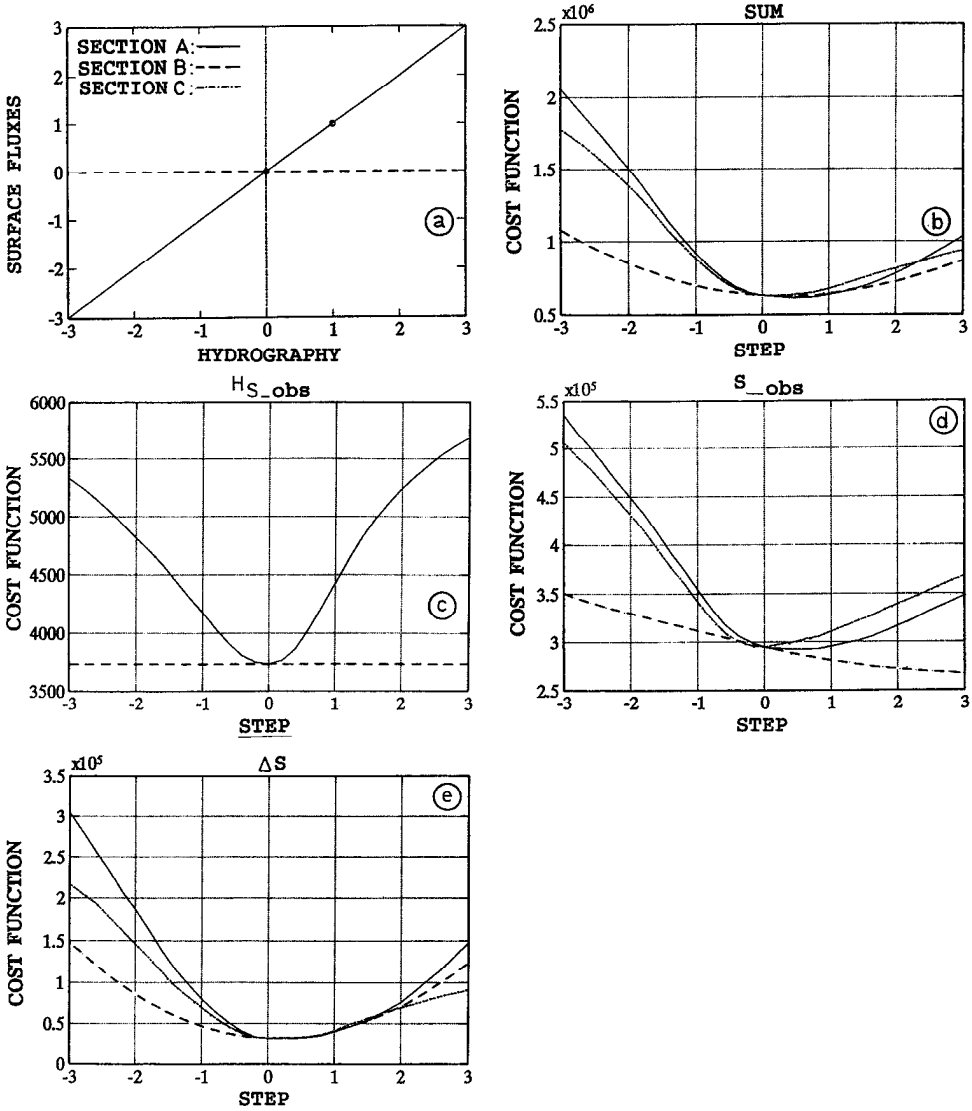
Figure 7. Sections of the parameter space of the cost function $J(X)$. The total amounts of the cost function values are denoted by "SUM." $H_{S,obs}$ are the cost function contributions from freshwater flux, S_{obs} from the model-data misfit of salinity and ΔS from temporal drifts of salinity, respectively. The contribution from $H_{T,obs}$, T_{obs} and ΔT are very similar to the salinity/freshwater curves and are omitted. (a) Schematic plot of the orientation of the sections presented in (b–e). Positions (0,0) and (1,1) mark both experiments S1 without and with noise added to the first guess, respectively.

reason for bad conditioning in our inverse model may be an underdetermination of the inverse problem due to dependent information contents in the data (with more unknowns than independent data). This causes a slower convergence of the cost function or a stalling of the minimization procedure with the consequence that the true minimum of the cost function cannot be found. Thus, apart from the minima presented in Figure 7, it is possible that another, global minimum for the cost function exists.

Although the results discussed above have been obtained only for a specific experiment (S1), the general results presented hereafter suggest that similar results would have been obtained when using another model configuration.

c. Surface fluxes. For inversions that are consistent with the observation errors of the data, the optimized surface fluxes should represent improved estimates for the thermohaline boundary conditions of this particular model. The possible improvement is based on the use of additional information, e.g. the comparatively better known temperature and salinity fields. The adjoint method applied here implicitly assumes that the model is capable of describing the real ocean state exactly. This assumption of an error-free model is usually not valid in oceanographic applications, as has already been pointed out for the Gulf Stream separation. Hence, the quality of the model influences the results of the minimization procedure. In Figure 8a the optimized surface heat flux of experiment L1 is shown. The extension and intensity of the regional heat uptake especially near the coast of Newfoundland is quite different from what can be seen in the observations (Fig. 2). This result is typical for non eddy-resolving GCMs of the North Atlantic circulation, especially when the boundary conditions use a Newtonian damping law (Sarmiento, 1986; Gerdes, 1988; see also Fig. 5a). The similarity between the optimized fluxes and a Newtonian relaxation arises from the indirect coupling of the thermohaline fluxes in the adjoint model to the surface hydrography through the Lagrange multipliers. Both, the optimized surface heat flux (Fig. 8a) and the surface temperature (not shown here) exhibit distinct differences to the observations off the Newfoundland coast. The data—model differences can be explained qualitatively with the cost function which shows that the observed heat loss is not compatible with the steady state demand for temperature. Reducing the steady state demand would result in a model state closer to the observations, but additionally this would imply larger temperature changes within one forward integration of the model. The reason for this model deficit has already been attributed to the southward extension of the Labrador Current. With the coarse model resolution the inverse model produces a quasi-steady state by allowing the model variables to deviate strongly from the observations. According to Böning (1992) this local problem disappears in an eddy-resolving model, because the northward displacement of the subarctic front represents the observed structures in a more realistic way.
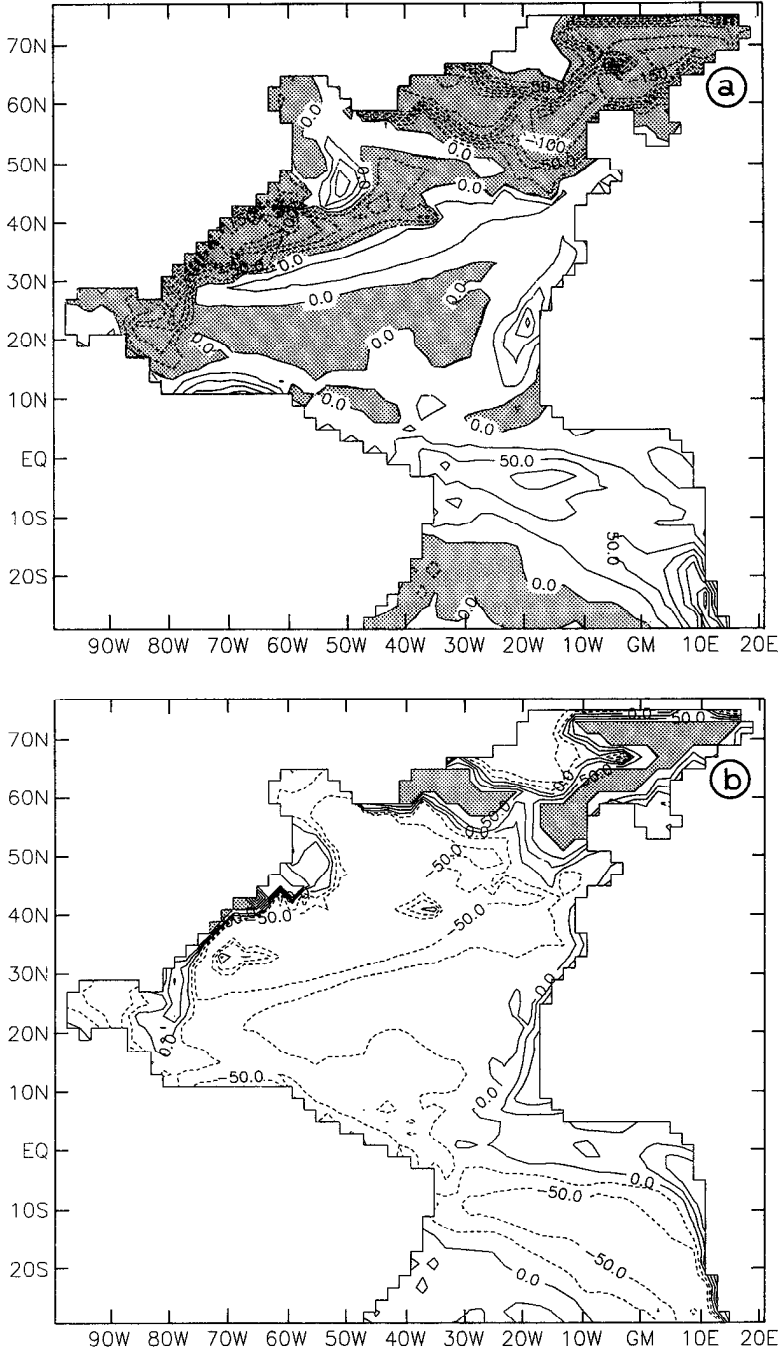
Figure 8. Exp. L1. (a) Optimized surface heat flux, negative areas are shaded. C.I. = 25.0 W/m². (b) data—model difference of the surface heat flux. C.I. = 25.0 W/m². Differences greater than 75.0 W/m² are shaded (flux limitation, see text).

Figure 8a displays the major regions of heat loss along the western boundary current (< -250 W/m^2) and between Greenland and the British Isles up to the northern model boundary (< -200 W/m^2). In the central subtropics of the northern hemisphere the surface fluxes reveal only a minor heat release to the atmosphere. It is this model area where the optimized surface fluxes are closest to the observations (Fig. 8b) and where the average values are near zero in accordance with the data of Isemer and Hasse (1987). Between the southern flank of the Gulf Stream extension area and the central subtropics a region of increased heat gain exists. The southward component of the Ekman transport causes a horizontal and diapycnal transport in the surface layers. Part of the cooled water masses of the Gulf Stream is heated in this region, and afterwards they recirculate in the southern part of the subtropical gyre (c.f. Fig. 16). The upwelling regions along the African coast show a heat gain of the ocean with a maximum off Namibia (> 175 W/m^2). Ranging from the Southwest African coast up to Northbrazil an area of heat gain can be seen, including the equatorial maximum. Except for the equatorial region, the heat gain in the remaining area is rather unrealistic, such that the data—model differences exceed -50 W/m^2 (Fig. 8b). One reason for these large differences along the South Equatorial Current (SEC) is the strong upwelling at the African coast, extending from about 20S to 35S that includes parts of the restoring zone in the South Atlantic of the model. Through an increase in the heat uptake the model tries to warm up the cold water masses of the thermocline and this tries to keep them close to the observations. The locally limited and observed heat gain along the African coast is not able to heat the water masses sufficiently, so that the region of heat uptake by the ocean is extended along the SEC.

The flux limitation explained at the beginning of this section is valid only in a small strip along the American coast and mainly in the subpolar regions (Fig. 8b). Both areas are marked by a strong heat release of the ocean, the model ocean tries to increase the heat loss in excess of what is observed.

It seems worthwhile to note that along the Gulf Stream extension area, in the northern part of the subtropical gyre and in the Labrador Sea the data—model differences are more than -50 W/m^2. In these parts and—with minor differences—in the central northern subtropics the heat loss is smaller for the optimized than for the observed heat fluxes. However, the optimized fluxes are still low enough to cause a cooling trend in the near-surface layers.

The optimized surface fluxes obtained with the hydrographic station data are not displayed here, because they exhibit similar large-scale features to the fluxes shown in Figure 8a. However, on a scale of only a few grid points, both thermohaline fluxes based on the optimization with station data show small-scale structures. This can be explained with the gradients that determine new estimates of the surface fluxes (Eq. 8 in SW95). The gradients consist of two terms, the data—model differences and the coupling to the model physics by the Lagrangian multipliers. The last term again

includes the data—model misfits of temperature and salinity. Although the model tries to produce smooth fields of the hydrography, when noisy hydrographic data are assimilated distinct data—model differences are introduced. These differences become visible even in the optimized surface fluxes through their indirect coupling via the adjoint equations to the data—model differences in the hydrography.

To summarize the results for the surface heat fluxes, the total rms-differences between optimized and observed values range between 42 W/m^2 and 57 W/m^2 for the experiments. The most significant large-scale deviations of the model heat fluxes from the observations arise in the subpolar area. Except for this region all other model parts tend toward a reduced heat release and/or an increased heat gain compared to the observations.

The optimized freshwater fluxes of experiment L1 displayed in Figure 9a reproduce the observed large-scale climatology. North of approximately 48N precipitation exceeds evaporation. Offshore the Irish coast and Newfoundland the fluxes exceed 2.0 m/y. By contrast, parts of the Gulf Stream area and its extension show strong evaporation excess causing a freshwater flux of −3.0 m/y. In the subtropics of both hemispheres evaporation is dominating the freshwater flux with more than −1.0 m/y in the North Atlantic and −2.5 m/y in the South Atlantic. The evaporation in the southern hemisphere is caused by the strong upwelling along the African coast. Similar to the heat fluxes the model tries to keep the less saline water masses close to the observations by increasing the evaporation. In accordance with the observations the equatorial freshwater flux reaches about −1.0 m/y.

Analogously to the data—model differences of the optimized heat fluxes the optimized freshwater fluxes show the greatest differences along the North American coast and in the northern model part (Fig. 9b). The largest area with maximum deviations extends from the North American coast to the Caribbean Sea and to the South American continent. The reason for the latter difference between data and model is not clear to us, however. In the named regions the flux limitation is active, but also in the major parts of the remaining model domain the optimized freshwater values tend toward an increased freshwater flux compared to the observations. Only along the flanks of the Gulf Stream and its extension, at the equator and in the Benguela Current region positive differences are visible, which is equivalent to an increased freshwater loss (evaporation excess) of the model ocean compared to the observations.

The freshwater fluxes exhibit area averaged rms-differences between observed and optimized values ranging between 0.9 m/y and 1.1 m/y for the experiments. The overall results demonstrate that especially in the western boundary current region, in the Caribbean Sea, the Gulf of Mexico and in the subpolar area the inverse model is unable to produce a picture of the freshwater fluxes that is consistent with the error estimates. In comparison with the observations all results of the inverse models are characterized by a decreased evaporation and/or an increased precipitation.
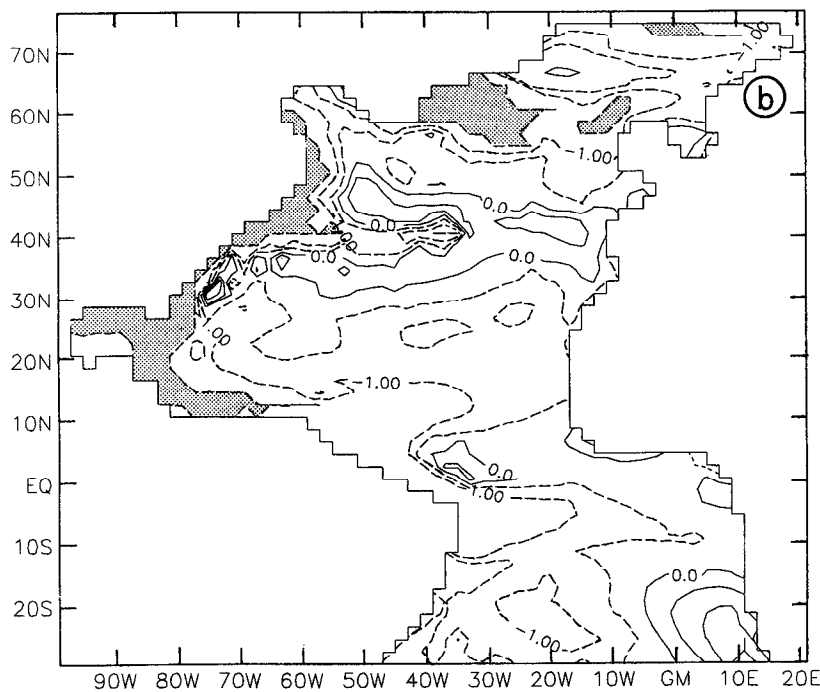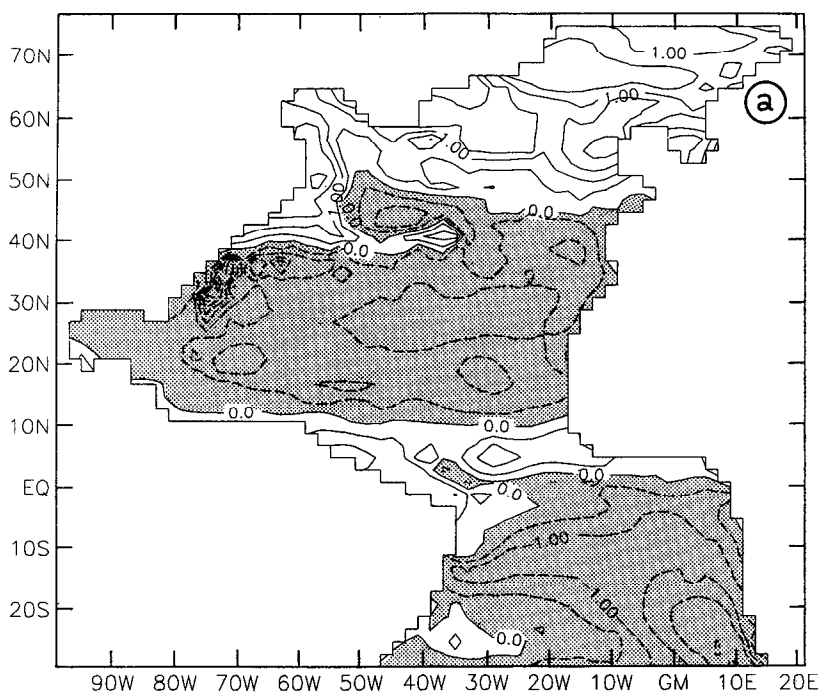
Figure 9. Exp. L1. (a) Optimized freshwater flux, negative areas are shaded. C.I. = 0.5 m/y. (b) data—model difference of the freshwater flux. C.I. = 0.5 m/y. Differences with 1.5 m/y are shaded (flux limitation, see text).

d. Hydrography. The fundamental hydrographic results obtained with the different inverse models show strong similarities over large parts, whereas distinct differences to the hydrographic observations are always evident. The differences in the hydrographic property distributions can be ascribed mainly to the chosen parameterization of diffusion. The most realistic distributions for the hydrographic fields may be expected with the isopycnal diffusion approach. Indeed, certain aspects of the results obtained with isopycnal diffusion are more reasonable than with the other mixing approaches. Therefore, we will focus our discussion on experiment S3 (Table 1).

The near-surface temperature at level 2 is displayed in Figure 10a. The arctic front at about 65N and the subarctic front at 45–50N are intensified compared to the smoothed hydrographic observations. The frontal structure at 50N exhibits strong gradients (6 °C and 2.7 psu). Due to the wrong model circulation along the Northeast American coast large data—model differences occur with maximum values of more than −10 °C (Fig. 10b) and −3 psu (Fig. 11b). In contrast to the other experiments, the model results with isopycnal diffusion show a realistic southward displacement of the Gulf Stream extension of about 500 km (Clarke *et al.,* 1980; Krauß, 1986). This may be explained by the reduced diapycnal mixing, so that stronger density gradients are found along the frontal region. From the Caribbean Sea to the Iberian peninsula a region of intensified temperature and salinity gradients marks the transition zone from strong heat release along the Gulf Stream/North Atlantic Current to the southward located area of heat gain and evaporation excess (Fig. 10a, 11a). The quantitative values for temperature and salinity east of the Midatlantic Ridge are, however, too warm and too saline, which is caused by a strong heat gain and evaporation excess. North of the subarctic front at about 50N, 40W the data—model differences reach more than −6 °C and 1 psu (Fig. 10b, 11b). These deviations can be explained by the position of the subarctic front at 40W and its subsequent northward displacement by about 1000 km (Krauß, 1986). The frontal structure in the model at this longitude is too far to the south.

As a general result, the optimized hydrography presented above shows a main thermocline that is too warm and salty along the northeast American coast, south of the NAC and near the equator. Though the influences of strong heat release and precipitation excess the Gulf Stream, the NAC, parts of the subtropics and particularly the subarctic region are too cold and less saline.

Another example that demonstrates the data—model differences common to all experiments is displayed in Figure 12. The section of potential temperature along 37N reveals some noisy structures even in the already smoothed hydrographic station data (Fig. 12a). Compared to the Levitus data (not shown) the gradients of the station data are intensified along the western boundary. Especially the experiments with isopycnal diffusion show an enhanced slope of the isotherms in this area (Fig. 12b). As a consequence of the flattening of the temperature isolines associated with the boundary current and the missing of cold slope water masses, the model
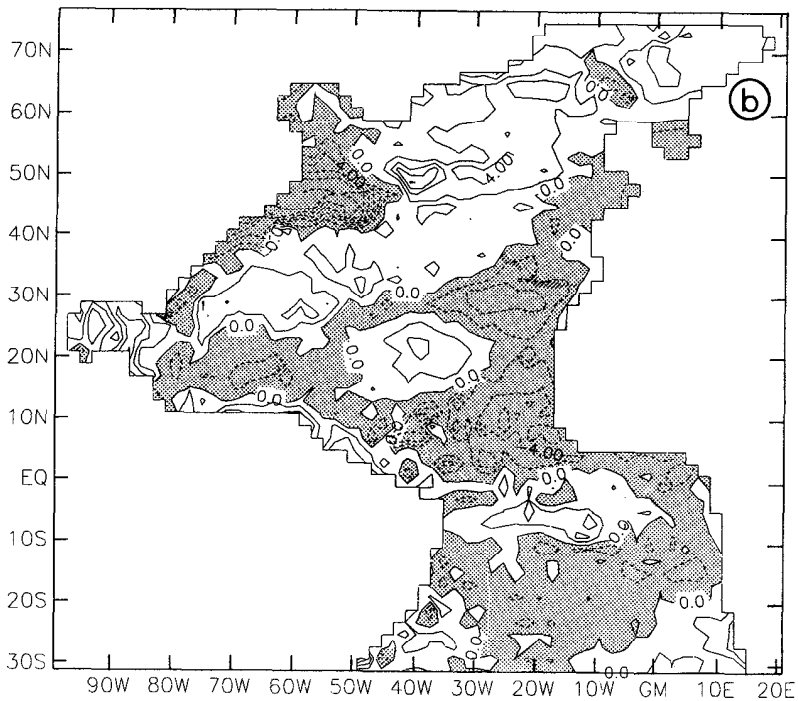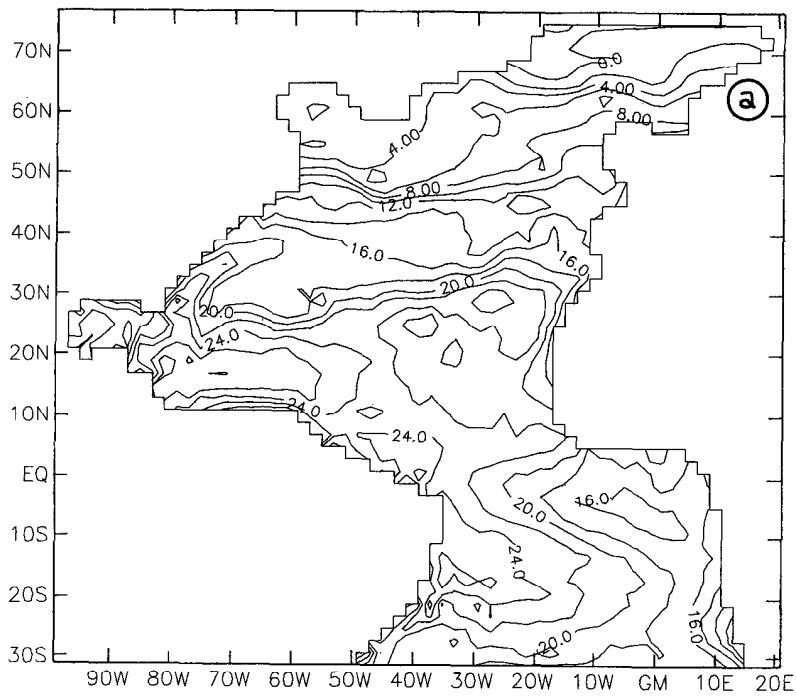
Figure 10. Exp. S3. (a) Optimized potential temperature at 81.5 m depth. C.I. = 2.0 °C. (b) data—model difference of potential temperature at 81.5 m depth, negative areas are shaded. C.I. = 2.0 °C. For optical reasons the difference between initial guess (≡ hydrographic station data plus Levitus data) and model is displayed.
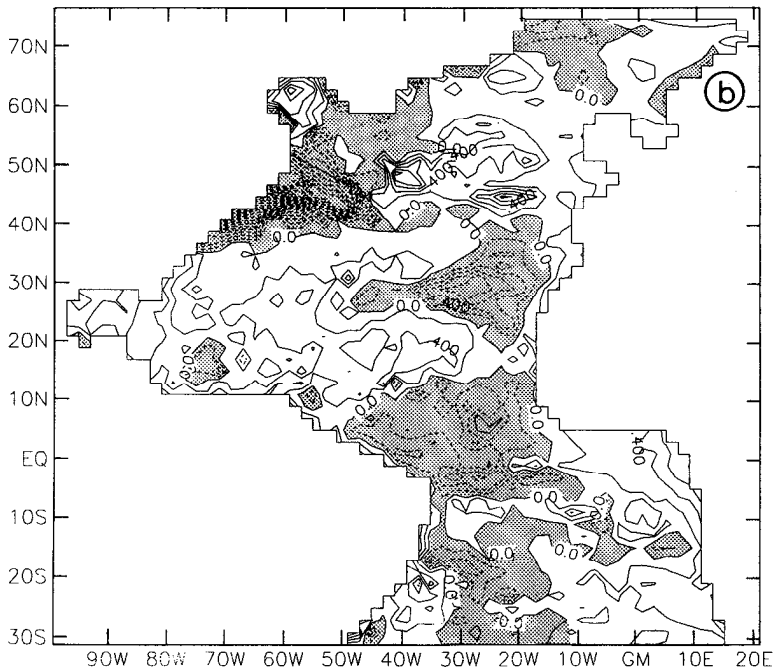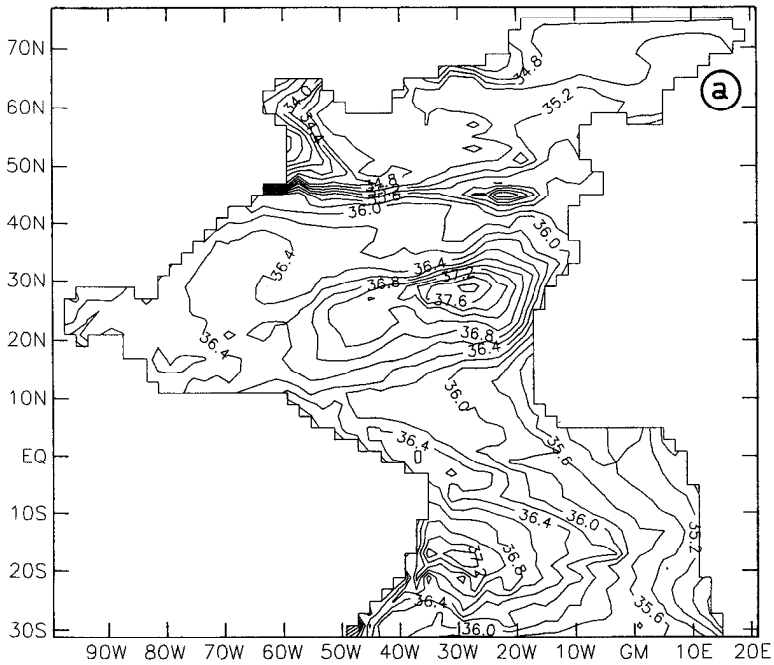
Figure 11. Exp. S3. (a) Optimized salinity at 81.5 m depth. C.I. = 0.2 psu. (b) data—model difference of salinity at 81.5 m depth, negative areas are shaded. C.I. = 0.2 psu. For optical reasons the difference between initial guess (≡ hydrographic station data plus Levitus data) and model is displayed.
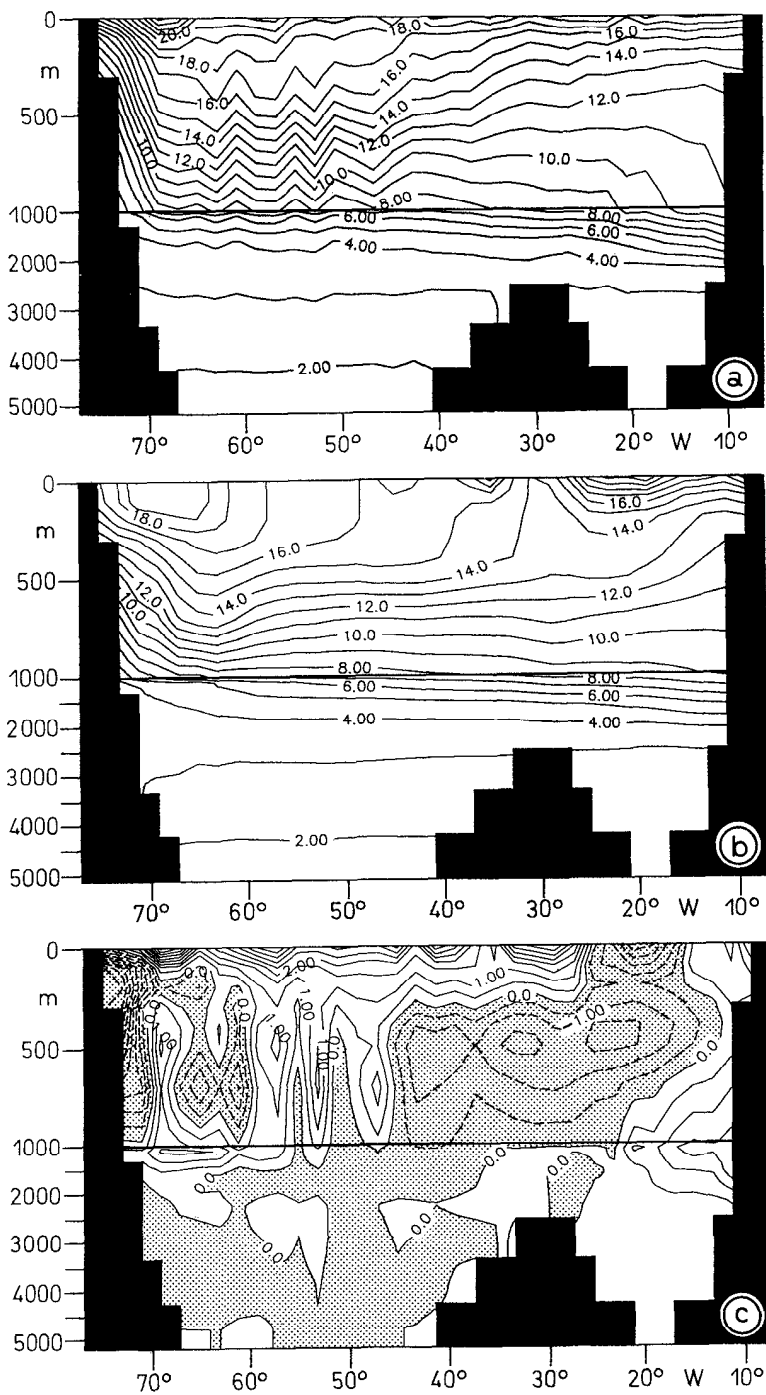
Figure 12. Potential temperature section along 37N. (a) Hydrographic station data. C.I. = 1.0 °C. (b) Experiment S3. C.I. = 1.0 °C. (c) data—model difference, experiment S3. C.I. = 0.5 °C.

temperatures are too high at the American coast (Fig. 12c). East of about 70W until 23W the near-surface water masses are much colder than in the observations. In particular, the near-surface temperature is almost constant in an area ranging from 40W to the western boundary current and down to approximately 400 m. This is a result of the strong heat release and evaporation such that the density increases and the near-surface water masses are convectively mixed and homogenized. East of this region the ocean gains heat and a shallow mixed layer develops. The noise in the data fields that can be seen in Figure 12a is caused by eddies which are found in a region from 45W to 65W. Thus, the data—model differences in the thermocline have alternating signs in this area. The warmer water masses in the thermocline of the inverse model extending from approximately the eastern boundary until 43W result from the heat gain of the ocean at this latitude and further northward. Through advection by the large–scale recirculation and by sinking these water masses can penetrate down to 1000 m. The temperature decrease at a depth of about 1000 m at the eastern boundary is a consequence of the missing Mediterranean outflow. Because this source is absent, the model produces a colder and less saline water mass than found in the observations.

Except for the differences caused by the noisy eddy fields below the surface layers no significant differences have been found in the optimized states along 37N for station data and Levitus data. We attribute this to the insufficient spatial and temporal resolution of the model.

Figure 13 displays the zonally averaged data—model differences of experiment S3 as a function of latitude. At the surface and north of 45N an area of too cold surface water can be seen, the signal penetrates down to a depth of 714 m. Below 1000 m and north of 50N the model ocean is too warm compared to observations. This is a consequence of the inaccurate representation of the Greenland—Scotland overflow system by the model; i.e. the coarse model resolution in combination with the smoothed hydrographic observations does not permit a realistic modelling of the overflow (c.f. Gerdes and Köberle, 1995). Moreover, the closed northern boundary and possibly the absence of any restoring to observations prevent a supply of cold arctic water masses to the deep model layers. The warm (and salty) anomaly around 45N that penetrates down to 714 m is caused by an unrealistic water mass structure east of Newfoundland and can be detected along the path of the NAC. In the central subtropics around 25N and in the equatorial region over large parts the thermocline between 159 m and 451 m is too cold and not saline enough, whereas the Northequatorial Current (NEC) is too warm and salty. Except for the northern model area, Figure 13 demonstrates that the assimilation procedure with a time scale of a few years to decades affects mainly the layers in the thermocline, whereas the deep hydrography is still close to the observations.

For the other experiments, the features differ substantially from Figure 13 only for the experiments with variable vertical diffusion (exp. L1, S1). In these experiments
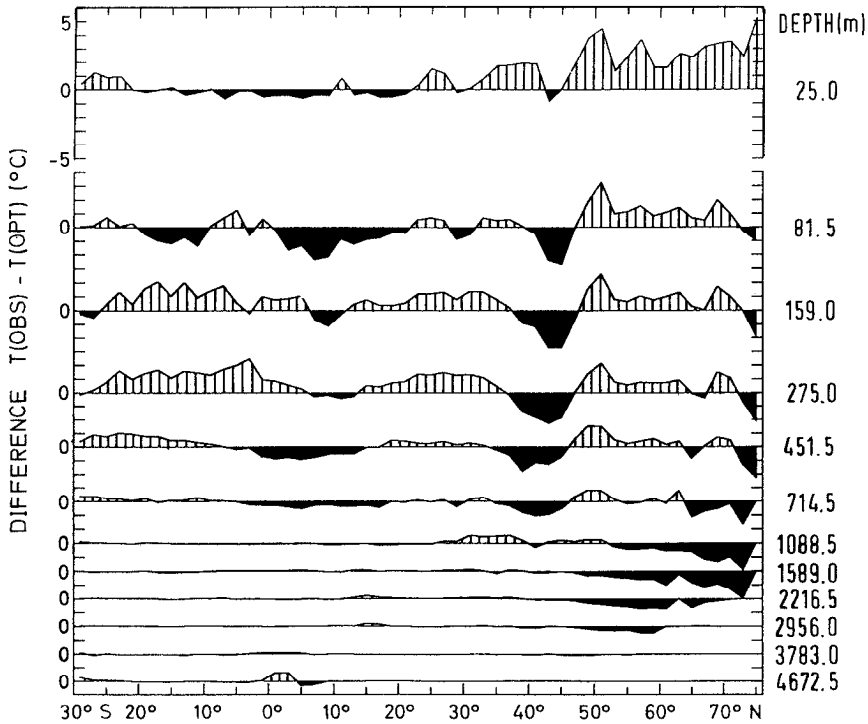
Figure 13. Zonally averaged data—model differences of potential temperature (°C). Exp. S3.

(not shown), especially in the South Atlantic the upper model layer is heated by insolation, whereas the second and third layers are by far too cold. Latitudinally averaged deviations are more than 8 °C. The cold and less saline water that stems from the upwelling region off Southwest Africa is heated in the surface layer along the path of the SEC. The warming increases the static stability, so that the density-dependent vertical diffusion coefficient on a large scale is smaller than 10^{-5} m²/s. In practice, the diffusive exchange across the boundary of the two uppermost layers is interrupted, while the vertical advection is too weak to compensate for this effect. Similarly, the subtropical evaporation excess increases the surface salinity. The density gain by evaporation is too weak, however, compared with the density loss by heating. Thus, the insulating effect through the small diffusion coefficient between first and second model layer is retained until the SEC reaches the equatorial current system.

The problem of isolated surface layers can principally be avoided by using larger vertical diffusion coefficients in the thermocline (c.f. exp. L2, S2). However, this would be contrary to the expected improvement when using vertically variable diffusion coefficients. Bryan (1987) showed, that a strong diffusion might cause a vertical water mass structure that is not consistent with observations.
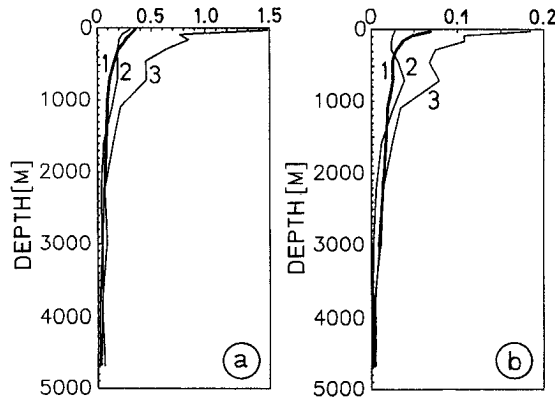
Figure 14. Horizontally averaged rms-differences of the temporal drifts after 5 years of integration time. (a) Potential temperature in °C and (b) salinity in psu. Curve *1: A priori* error estimates $\sigma_{\Delta T, \Delta S}$, curve 2: exp. L2, curve 3: exp. S1.

The horizontally averaged rms-residuals of the temporal drifts for a 5-year integration time are presented in Figure 14. The curves are shown for the experiment with the smallest (L2) and largest (S1) temporal drifts, respectively. For L2, the rms-residuals show an overall agreement with the a priori temporal error estimates, thus indicating a quasi-stationary model ocean. In S1, however, in the upper model layers large deviations from the *a priori* errors are obvious. They are caused by large temporal drifts along the subarctic front and on the Newfoundland shelf. Other experiments show distinct temporal residuals in isolated model parts, such as the Gulf of Mexico and the North Sea. The geographical distributions of the temporal residuals in all experiments are quite noisy. A typical picture of the temperature differences between final and initial model state is given in Figure 15 for experiment S3, showing temporal drifts with alternating signs along the subarctic front. At the southern flank of the Gulf Stream and at the African coast a cooling tendency is visible, while the central northern subtropics get warmer throughout the integration period of five years. It is important to note that the time rates of change for other parts of the model are small, thus indicating that the rms-residuals are smaller than the temporal *a priori* error estimates.

e. Mean circulation. The velocity field adapts geostrophically to the optimized hydrographic distributions. Below the thermocline, the optimized temperature and salinity arrays are still close to their initial fields, i.e. close to the observations. Because of this and the constant wind forcing for the external mode of the model velocity, differences between the experiments are hardly detectable at greater depths.

As an example for the near-surface circulation Figure 16 shows the velocity field for exp. L3 at a depth of 81.5 m. The large-scale features of the subpolar gyre as well
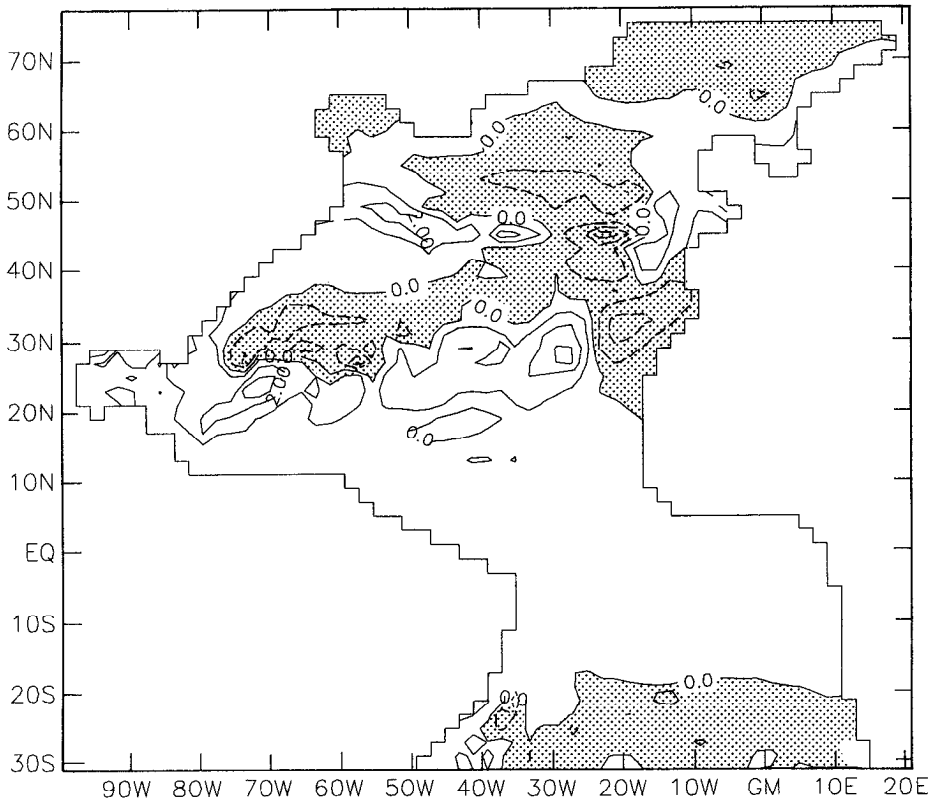
Figure 15. Potential temperature at 81.5 m depth. Temporal drift of optimized state: $T^f - T^0$ (exp. S3). C.I. = 1.0 °C. Negative areas are shaded.

as the western boundary currents (Gulf Stream, Brazil Current), the NAC, the North Equatorial Counter Current (NECC) and the SEC are clearly visible. The subtropical recirculation of the northern hemisphere covers the greatest part of the Atlantic with weak eastern boundary currents and a stronger North Equatorial Current (NEC). The details differ, however, clearly from what is known from velocity observations. In the model no counter current inshore the Gulf Stream exists, that would be able to transport cold and low salinity water southward. The coarse resolution and the missing seasonal forcing are also responsible for the extremely broad NECC. At 36N the Gulf Stream was found to be limited to a depth range above 1500 m and the transports vary between 76.0 and 89.6 Sv (Table 3), whereas Leaman *et al.* (1989) report transports at Cape Hatteras (35N) of about 93.7 Sv down to the bottom.

In all experiments the surface to deep water conversion is located southeast of Greenland in the Irminger Sea and, to a lesser extent, in the Norwegian Sea. The former region is the source of the deep western boundary current (DWBC) of the model (Fig. 17). The overflow across the Greenland-Scotland ridge system that
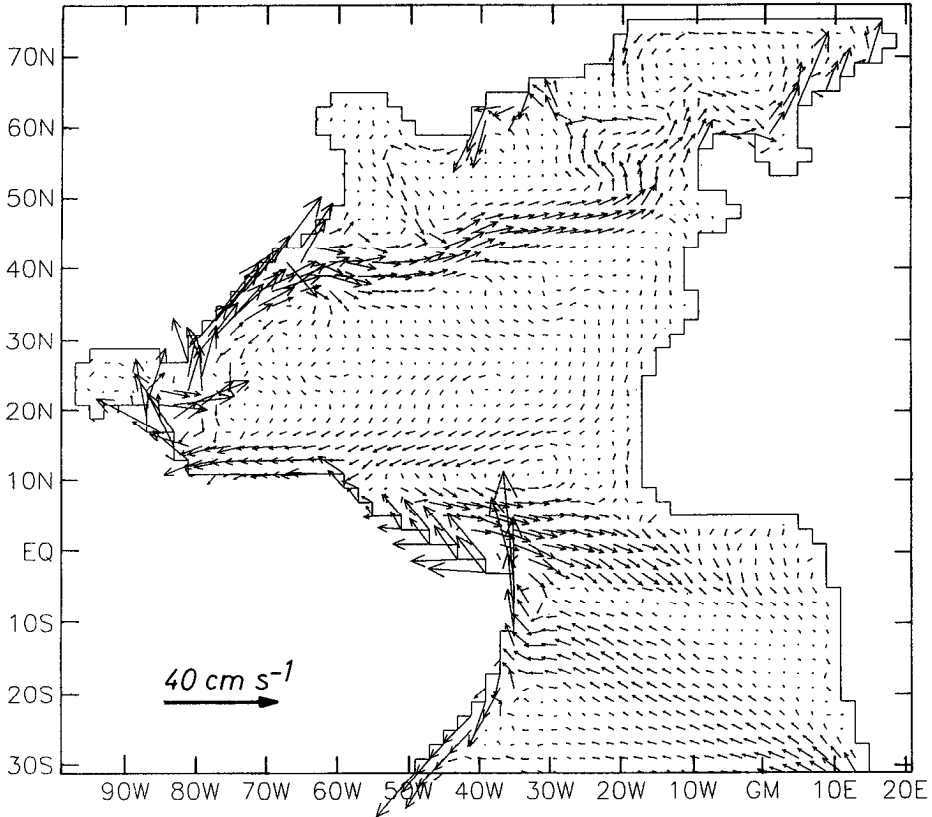
Figure 16. Velocity at 81.5 m depth (level 2). Exp. S3.

amounts to 3–4 Sv in the model is too small compared to observations (5.6 Sv, Dickson *et al.*, 1990). This deficit of the model is mainly due to the coarse model resolution, although in the unsmoothed hydrographic data the overflow signal is detectable. The spreading of the DWBC between 40N and 60N is rather unrealistic

Table 3. Transports of Gulf Stream and Deep Western Boundary Current (DWBC), computed from the coast to the zero line of the meridional velocity component. Typical values for the width of the boundary currents are 10°. Depth range for Gulf Stream: 0–1306 m. Depth range for DWBC: 1306 m–bottom.

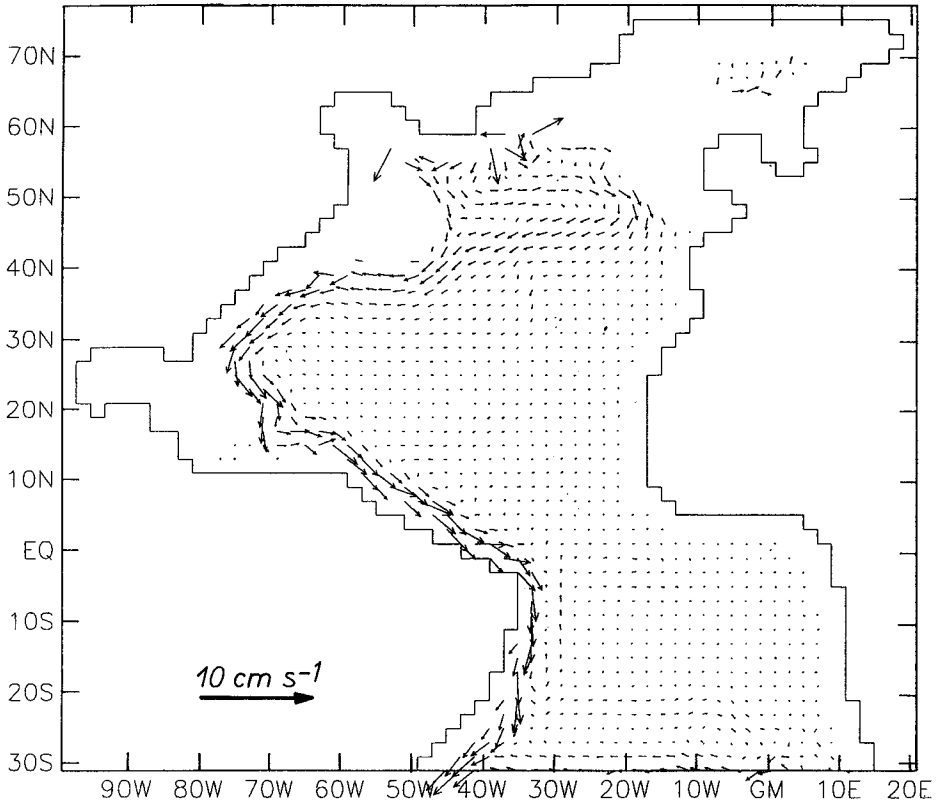| Experiment	Gulf Stream		DWBC	
	36N	36N	24N	20S
L1	78.3	23.5	18.1	13.6
L2	88.2	28.5	19.5	13.8
L3	76.0	22.3	18.3	15.3
S1	84.1	28.5	17.4	13.8
S2	89.6	34.2	20.9	7.6
S3	77.6	22.1	14.6	13.7

Figure 17. Velocity at 2216.5 m depth (level 9). Exp. S3.

and not consistent with recent theories about the deep circulation based on observa-
tions (Smethie and Swift, 1989; McCartney, 1992). At 36N, the southward DWBC
transport ranges between 22.1 and 34.2 Sv, depending on the model version (Table 3)
and extending up to 14° offshore which seems to be rather unrealistic. Recent
observation show a variety of values for the DWBC transports that lie between 8 Sv
(Fine and Molinari, 1988) and 35 Sv (Leaman and Harris, 1990). Although the
DWBC transport of the model lies within the observed range, the model velocities of
the DWBC (1–2 cm/s) are too small compared to observed values (5–30 cm/s, Lee *et
al.* 1990; Rhein, 1994; Rhein *et al.* 1995).

The zonally integrated volume transport displayed in Figure 18 is qualitatively
consistent with the classical picture of the thermohaline overturning. Maximum
values are between 16 and 23 Sv in the different experiments (Table 4). The transport
in the near surface layers at the equator is dominated by Ekman divergence, which
causes an upwelling of about 10 Sv. At 60N about 14 Sv of the warm water sphere are
transformed to NADW, spreading southward above 3000 m depth. However, only a
reduced amount of deep water leaves the southern boundary of the inverse model at
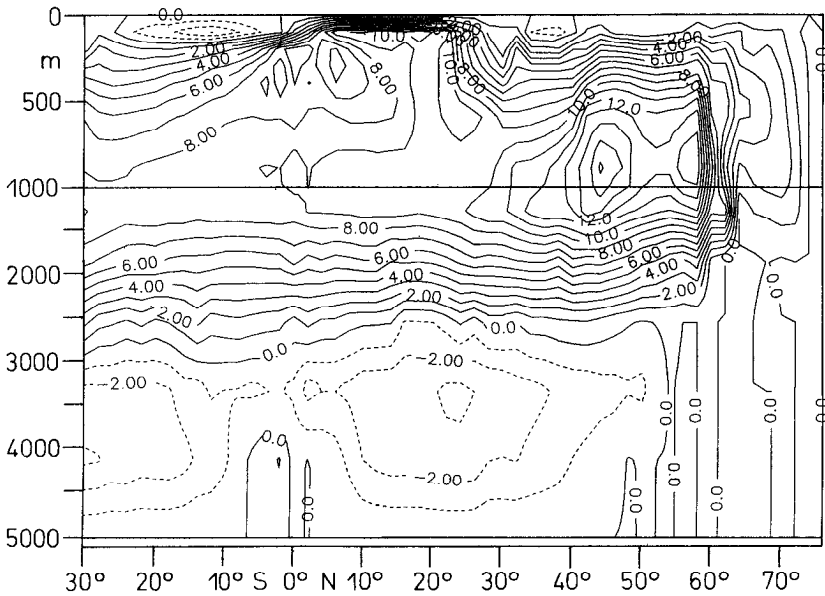
Figure 18. Meridional overturning stream function (Sv), final state of exp. S3. C.I. = 1.0 Sv.
Positive values denote clockwise rotation.

30S. This is due to an artificial mid-latitude upwelling between 30N and 45N, associated with a southward decrease in overturning strength. Recent results from an investigation of different model configurations by Böning *et al.* (1995) showed that the mid-latitude upwelling depends on the horizontal resolution and mixing param-eterization. Use of a new parameterization for eddy-induced tracer transports (Gent and McWilliams, 1990, Gent *et al.*, 1993) reduces the upwelling significantly, thus increasing the transport rates of the NADW south of 30N (Böning *et al.*, 1995).

In all experiments AABW flows northward below 4000 m depth across the southern boundary (3 Sv in Fig. 18). Between 1300 m and 4000 m depth 12 Sv of NADW leave the part of the model area shown here. Above 1300 m approximately 9

Table 4. Meridional overturning (Sv) at 43N (Maxima), 25N and 29S (southern boundary of inverse model).

| | Overturning (Sv) | | |
Experiment	43N	25N	29S
L1	19.4	13.2	10.3
L2	19.7	12.5	6.8
L3	16.2	12.6	10.2
S1	20.3	13.1	10.4
S2	23.1	14.0	7.0
S3	16.2	10.4	9.1

Sv of AAIW and surface water enter the northern model domain. Based on inverse calculations, Rintoul (1991) computed an export of NADW across 32S of 17 Sv, that is compensated by northward transports of surface water (8 Sv), AAIW (5 Sv) and AABW (4 Sv). Even taking into account an error of ±2 Sv in Rintoul's numbers, the results of our inverse model seem to be too small. The overturning and deep water formation in the North Atlantic interacts with the transport across the southern buffer zone at 30S. The restoring of the South Atlantic hydrography to Levitus data, as it was done here, seems to be problematic and results in too weak transports not only across 30S but also for the whole northern model area. To improve such transport estimates across open model boundaries an optimization of these transports as additional control variables in the adjoint formalism promises to be a better approach.

To investigate the influence of different wind stress fields on the inverse solutions and especially on the mean circulation, we performed several experiments with the ECMWF wind stress fields (Trenberth *et al.*, 1989). The vertically integrated volume transports did increase locally by more than 30% (e.g. in the Gulf Stream recirculation area) compared to the Hellerman and Rosenstein (1983) wind stresses. Despite this fact, however, the overall effect on the thermohaline circulation was rather small with a change in the cost function value of less than 5%. The results demonstrate that the optimized thermohaline model parameters are nearly insensitive to different wind fields. In retrospect, this can be interpreted as an additional justification for the validity of our simplified adjoint approach without optimizing the wind stress and velocity.

f. Heat transport. Based on hydrographic data, Hall and Bryden (1982) computed an overturning at 25N of 18 Sv, whereas the maximum value in our experiments is 14 Sv. As a consequence of the too weak overturning cell (Table 4) the northward heat transport is weaker than required by observations. To demonstrate the different performances of our experiments, Figure 19 shows the results for the experiments with the smallest (L1) and largest northward heat transports (S2). Due to the different overturning rates notable differences in the heat transports occur. Especially in Figure 19b the total heat transport shows a rather unrealistic southward heat transport at the southern boundary. At the equator, in both experiments the heat transport is northward and about 0.65 PW (1 PW = 10^{15} W). The maximum values for the heat transports are 1.07 PW at 26N (S2) and 0.83 PW at 18N (L2), compared to 1.2 PW at 25N from Hall and Bryden (1982).

In an exact steady state the integrated surface heat flux balances the northward transport of heat, thus the temporal change of the ocean heat content equals zero. In our case, however, we have only a quasi-steady state with non-vanishing temporal drifts (cf. Fig. 15). In all experiments a tendency of an ocean warming exists, that is equivalent to a heat loss through the surface at high latitudes which is too small
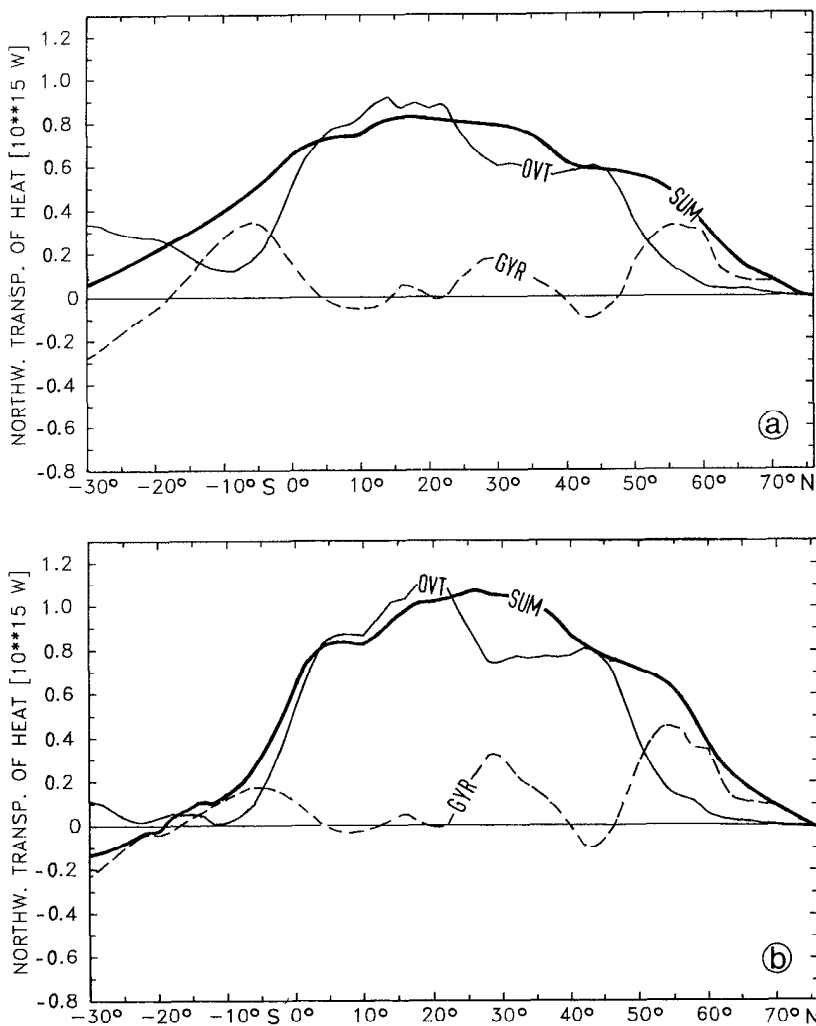
Figure 19. Northward heat transport (PW) as a function of latitude. (a) Exp. L1, (b) Exp. S2. SUM: total transport, OVT: Overturning contribution, GYR: Horizontal gyre contribution.

compared to the heat gain at low latitudes. For example, in exp. S2 about 0.3 PW of the northward heat transport are used to heat the water masses of the North Atlantic. This warming tendency is, however, not contrary to the aforementioned results concerning the thermocline hydrography, which is characterized in large parts by a cooling effect. Maximum values for the volume averaged warming in the ocean are 0.05 °C in five years.

g. Freshwater transport. In addition to the experiments S(1–3) and L(1–3) one experiment was performed in order to establish the sensitivity of the inverse model to

the freshwater transport. Experiment L1 was repeated including Mediterranean salt flux (i.e. restoring to Levitus data near the inflow) and river runoff from the Amazonas (Baumgartner and Reichel, 1975). In the oceanographic literature different definitions for freshwater transport exist (e.g. Wijffels *et al.*, 1992). We will use it as a pseudonym for the term that in the steady state compensates the salinity changes caused by evaporation, precipitation and river runoff. Fig. 20 displays the freshwater transports of Baumgartner and Reichel (1975), Schmitt *et al.* (1989) and the value of Hall and Bryden (1982) at 25N. The values of the first and second authors were obtained by integrating the surface freshwater fluxes, including river runoff and Mediterranean salt flux into the North Atlantic. The curves denoted by "A" and "B" show the transports that were obtained with our inverse procedure without and with river runoff plus Mediterranean salt flux, respectively. In the subpolar Atlantic all results show a southward transport of freshwater, caused in the observations by freshwater supply through the Bering Strait and by precipitation excess as well as river runoff in the Arctic that amounts to -0.1 Sv in total (Coachman and Aagaard, 1988). At the southern open boundary, model and observations reveal a northward freshwater transport, caused by the maximum of evaporation excess at about 10S (cf. Fig. 9a). In the equatorial region of the model the freshwater transports become southward—contrary to the observations—, because precipitation exceeds evaporation (and river runoff in case "B") (cf. Fig. 9a). North of 10N until 35N the offset between the curves "A" and "B" is nearly constant, indicating a decrease in southward freshwater transport due to the Mediterranean inflow. Although the freshwater transports of the inverse model reveal curves similar to the observed ones, their absolute values and partly also their signs differ substantially from the observations. The inverse model tries to freshen the sea surface by increasing the precipitation and/or reducing the evaporation, thus producing smaller northward freshwater transports.

A systematical difference between model values and observed freshwater transports is based on the temporal changes in salinity. Integrating the surface freshwater fluxes yields a value at 30S that is about 0.2 Sv above the directly computed freshwater transport. Although this transport (dotted curve in Fig. 20) approximately follows the observations, it indicates a volume averaged salinity increase of 0.005 psu within 5 years. This effect is identical to the warming tendency. The northward transport of salt is not compensated by an equivalent freshwater gain through the surface (despite the fact that the surface is already fresher than the observations).

An estimate for the confidence intervals of the inverse solution can be determined with the Hessian matrix. It is defined as the second derivative of the cost function with respect to the control variables. The inverse of the Hessian matrix is the error covariance matrix of the optimized model parameters. However, computing the Hessian and its inverse is not yet computationally feasible for problems of the
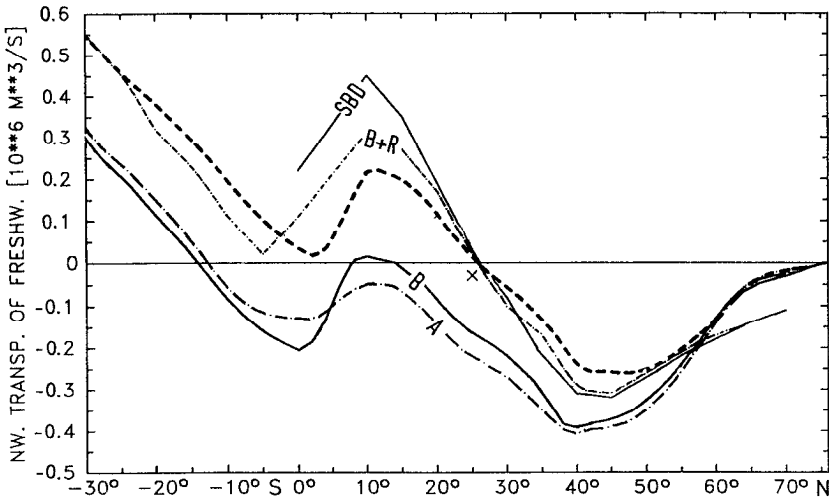
Figure 20. Northward freshwater transport (Sv) as a function of latitude. Curve "A": Exp. L1, curve "B": Exp. L1 with Amazonas runoff (0.19 Sv, Baumgartner and Reichel, 1975) and with restoring to Levitus data at the Mediterranean inflow. Dotted line: Integrated surface freshwater flux (Exp. L1 with Amazonas runoff and Mediterranean restoring). SBD: Schmitt *et al.* (1989), B+R: Baumgartner and Reichel (1975), ×: Hall and Bryden (1982).

dimensionality of our inverse problem ($10^4 - 10^5$ control variables). Instead a simplified approach was used to calculate at least approximately the diagonal elements of the Hessian matrix at certain locations in the model. This approach may not be strictly correct and representative, but it still gives some information on the formal error fields that can be expected when applied to the whole model. The matrix was determined by an approximation to the cost function gradients (Tziperman and Thacker, 1989). Computation of the finite differences of the first derivatives of the cost function J with respect to the variables α_i yields the approximated Hessian matrix:

$$\frac{\partial^2 J}{\partial \alpha_i \partial \alpha_j} \approx \left(\left. \frac{\partial J}{\partial \alpha_i} \right|_{\alpha_j + \Delta \alpha_j} - \left. \frac{\partial J}{\partial \alpha_i} \right|_{\alpha_j} \right) \frac{1}{\Delta \alpha_j}. \tag{3}$$

The largest uncertainties found for the heat and freshwater fluxes were 32.1 W/m² and 0.24 m/y, respectively. The maximum errors for temperature and salinity were found in the upper ocean with 0.93 °C and 0.23 psu, respectively. The overall errors for the hydrography and the surface fluxes are by far too small compared to the large data—model differences, indicating that the systematic uncertainties like a local cost function minimum have not been taken into account by this simplified computation (c.f. Marotzke and Wunsch, 1993).

5. Discussion and conclusions

The inverse approach presented in this paper is one of the first attempts combining data and complex GCMs to get large–scale models closer to observations. A simplified adjoint method has been applied to assimilate Levitus data and hydrographic station data into different versions of an Atlantic GCM based on the full set of primitive equations. The effort was intended to produce optimal results for the hydrography, for the air-sea fluxes and indirectly, for the circulation.

With two preliminary experiments presented in Section 3 it has been shown that neither forcing the ocean with thermohaline fluxes based on observations nor restoring the surface hydrography to prescribed values could produce a realistic model state for both the surface fluxes and the hydrography. Compared to these results, the inverse solutions look better than either prognostic run.

However, the final state of optimization produced a picture of the circulation and the hydrographic distributions (formally) inconsistent with observations and the requirement of a steady state. In SW95 we discuss the problems related to local minima in the cost function. We cannot exclude that with the shown experiments only local minima have been found instead of the global minimum. The use of approximate adjoint equations instead of a complete adjoint model may support this possibility. The experiments rather suggest, however, that the incompatibilities of the steady state model with the hydrographic observations and the surface fluxes are responsible for the unrealistic results over large parts of the ocean.

It has already been noted, that in particular the experiments with hydrographic station data produced contributions to the cost functions that were notably larger than the expected errors. This can be attributed to too small observation errors deduced from the hydrographic station data. If the cost function values for the solution of hydrographic station data are evaluated using Levitus' error estimates, the final cost function values are smaller and similar to those obtained for the Levitus data. However, relaxing the observation errors would produce larger data—model differences, probably exceeding observed annual amplitudes of temperature and salinity (c.g. Levitus, 1984). Particularly the station data are biased toward the summer season, in contrast to the tendency of the model to produce a "winter" state over large parts, thus further increasing the deviations from the observations.

With respect to the cost function results shown in Table 2, the experiments with Levitus data formally produced the best results. Nevertheless, there exists no experiment (even with Levitus data) that represents without any restriction the "best" one, producing a plausible picture of all, the hydrography, the circulation and the forcing fields. The structure of the near-surface hydrography was determined mainly by the different choices of diffusion rather than the different hydrographic data sets. An experiment with isopycnal diffusion (exp. S3) that contained some more realistic aspects than the other realizations was investigated in more detail in Section 4. In all experiments along the subarctic front, the African coast and in the SEC a

distinct sensitivity of the hydrography on the mixing parameterization has been found. The experiments showed that serious problems (numerically as well as physically) may arise in the near surface layers for time-invariant surface fluxes. This is especially true for the experiments with stability dependent vertical diffusion coefficients (exp. L1, S1), where small diffusion coefficients prevented an effective water mass exchange between the upper layers of the ocean. The results reveal that an improved model should include the optimization of diffusion coefficients.

Marotzke and Wunsch (1993) obtained quite similar results to ours with a somewhat different prognostic/adjoint model and a different data set. Their model used simplified momentum equations; the local time derivative and advection of momentum have been neglected; and Rayleigh friction instead of horizontal and vertical eddy viscosity parameterizations have been used. The authors report on problems related to the simplifications in their model. In their experiments the locally acting Rayleigh friction caused noisy optimized velocity fields, whereas in our experiments, through the non-local effect of the Laplacian friction, the velocity fields look rather smooth.

Due to the smaller meridional model extension (9.5N to 59.5N) in Marotzke and Wunsch (1993) the deep water formation in their experiments was mainly caused by the restoring of the model hydrography to the observed hydrographic data. Therefore, no extreme heat releases around 60N like in our experiments (Fig. 8) can be found along the northern model boundary in the results of Marotzke and Wunsch.

The heat transports obtained with our experiments are considerably larger than those of Marotzke and Wunsch, at a similar horizontal resolution. These differences are caused by higher maximum values of the part of the heat transport attributable to the meridional overturning, e.g. 0.9 PW in Figure 19b at 25N compared to 0.33 PW at 27.5N as reported by Marotzke and Wunsch. It seems worthwhile to note that the maximum transport in experiment S2 (Fig. 19b) is within the error estimates of the Hall and Bryden (1982) value, and higher than the transports obtained with Levitus data. One has to keep in mind, however, that S2 is the experiment with the largest heat transport of all realizations. The other experiments with hydrographic data show similar overturning rates and thus heat transport values close to those obtained with Levitus data. About 0.3 PW of the total heat transport in experiment S2 are used to warm up the water masses in the North Atlantic, thus reducing the number of 1.07 PW to a smaller value in a steady state.

The model hydrography reproduced the observed distributions on a large scale. Regionally, however, distinct differences to the observations became obvious. In particular, the dynamically active areas of the western boundary current and the subpolar region showed strong misfits between hydrography and surface fluxes. The front associated with the Gulf Stream is known to be highly variable in time and space. Thus, especially this area would likely benefit from a seasonal forcing and an

increased spatial resolution, because the spatial hydrographic structure and its temporal variability present in observations could be better resolved by the model.

Due to the high computational burden for an inverse model like ours with increased horizontal resolution, we performed only a few experiments with a vertically increased resolution (48-layers) of the inverse model. The computational burden, however, was still so excessive that we had to restrict the integration time. Nevertheless, the results indicated that neither in the Gulf Stream area nor in the other parts of the model an increase of the vertical resolution alone gives better results, i.e. smaller cost function values. Therefore, it seems to be important to increase both the three-dimensional spatial as well as the temporal resolution.

Increasing the spatial resolution of a primitive equation model and its adjoint up to an eddy-resolving scale, although still a technical challenge, seems to be attainable with ongoing developments in computer technology. In particular, this might improve the model estimates in overflow regimes (e.g. Denmark Strait), provided that hydrographic data exist. Variable and small transport estimates across the southern open boundary at 30S shown in Table 4 require an estimation within the optimization formalism with the ultimate aim to increase the meridional overturning and the heat transport on a basin scale.

Expanding the temporal and spatial resolution will require more data to obtain a model state close to the observations. All available data, such as observations of tracers, nutrients and altimetric observations as well as current meter measurements should be used to get a complete picture of the ocean state. The result of the inversion should give quantitative estimates which of these data are redundant or not consistent with other observations. In addition to the data, it seems to be necessary to include improved a priori error estimates as covariances into the optimization procedure.

REFERENCES

Baumgartner, A. and E. Reichel. 1975. Die Weltwasserbilanz. Oldenbourg, München, 179 pp.
Böning, C. 1992. Transportprozesse im subtropischen Nordatlautik: Untersuchumgen mit wirbelauflösenden Modellen der windgetriebenen und thermohalinen Zirkulation, Habilitation, Christian-Albrechts Universität Kiel.
Böning, C. W., W. R. Holland, F. O. Bryan, G. Danabasoglu and J. C. McWilliams. 1995. An overlooked problem in model simulations of the thermohaline circulation and heat transport in the Atlantic Ocean. J. Climate (in press).

Bryan, F. 1987. Parameter sensitivity of primitive equation ocean general circulation models. J. Phys. Oceanogr., *17*, 970–985.

Bryan, K. 1969. A numerical method for the study of the circulation of the world ocean. J. Comput. Phys., *4*, 347–376.

Bunker, A. F. 1976. Computations of surface energy flux and annual air-sea interaction cycles of the North Atlantic Ocean. Mon. Weath. Rev., *104*, 1122–1140.

Clarke, R. A., H. W. Hill, R. F. Reininger and B. A. Warren. 1980. Current system south of the Grand Banks of Newfoundland. J. Phys. Oceanogr., *10*, 25–65.

Coachman, L. K. and K. Aagaard. 1988. Transports through Bering Strait: annual and interannual variability. J. Geophys. Res., *93*, (C12), 15535–15539.

Cox, M. D. 1984. A primitive equation, 3-dimensional model of the ocean. GFDL Ocean Group Tech. Rep. No. 1, GFDL/Princeton University.

—— 1987. Isopycnal diffusion in a *z*-coordinate ocean model. Ocean modelling, unpublished manuscript, *74*, 1–5.

Cox, M. D. and K. Bryan. 1984. A numerical model of the ventilated thermocline. J. Phys. Oceanogr., *14*, 674–687.

Cummins, P. F., G. Holloway and A. E. Gargett. 1990. Sensitivity of the GFDL Ocean General Circulation Model to a parameterization of vertical diffusion, J. Phys. Oceanogr., *20*, 817–830.

Dickson, R. R., E. M. Gmitrowicz and A. J. Watson. 1990. Deep-water renewal in the northern North Atlantic. Nature, *344*, 848–850.

Dorman, C. E. and R. H. Bourke. 1981. Precipitation over the Atlantic Ocean, 30S to 70N, Mon. Weath. Rev., *109*, 554–563.

Fine, R. A. and R. L. Molinari. 1988. A continuous deep western boundary current between Abaco (26.5N) and Barbados (13N), Deep-Sea Res., *35*, 1441–1450.

Gargett, A. E. 1984. Vertical eddy diffusivity in the ocean interior, J. Mar. Res., *42*, 359–393.

Gargett, A. E. and G. Holloway. 1992. Sensitivity of the GFDL ocean model to different diffusivities for heat and salt, J. Phys. Oceanogr., *22*, 1158–1177.

Gent, P. R. and J. C. McWilliams. 1990. Isopycnal mixing in ocean circulation models. J. Phys. Oceanogr., *20*, 150–155.

Gent, P. R., J. Willebrand, T. J. McDougall and J. C. McWilliams. 1995. Parameterizing eddy-induced tracer transports in ocean circulation models. J. Phys. Oceanogr., (in press).

Gerdes, R. 1988. Die Rolle der Dichtediffusion in numerischen Modellen der Nordatlanti-schen Zirkulation, Berichte aus dem Institut für Meereskunde an der Christian-Albrechts-Universität Kiel PhD thesis. No. 179, pp. 176.

Gerdes, R. and C. Köberle. 1995. On the influence of DSOW in a numerical model of the North Atlantic general circulation. J. Phys. Oceanogr., (in press).

Gerdes, R., C. Köberle, and J. Willebrand. 1991. The influence of numerical advection schemes on the results of ocean general circulation models. J. Clim. Dyn., *5*, 211–226.

Hall, M. M. and H. L. Bryden. 1982. Direct estimates and mechanisms of ocean heat transport, Deep-Sea Res., *26*, 339–359.

Haney, R. L. 1971. Surface thermal boundary condition for ocean circulation models, J. Phys. Oceanogr., *1*, 241–248.

Hellerman, S. and M. Rosenstein. 1983. Normal monthly wind stress over the world ocean with error estimates. J. Phys. Oceanogr., *13*, 1093–1104.

Hogg, N. G. 1987. A least-squares fit of the advective-diffusive equations to Levitus Atlas data. J. Mar. Res., *45*, 347–375.

Hsiung, J. 1986. Mean surface energy fluxes over the global ocean. J. Geophys. Res., *91,* (C9), 10585–10606.

Isemer, H.-J. and L. Hasse. 1987. The Bunker climate atlas of the North Atlantic Ocean, *2,* Air-Sea Interactions, Springer Verlag.

—— 1991. The scientific beaufort equivalent scale: effects on wind statistics and climatological air-sea flux estimates in the North Atlantic Ocean. J. Climate, *4,* 819–836.

Isemer, H.-J., J. Willebrand and L. Hasse. 1989. Fine adjustment of large scale air-sea energy flux parameterizations by direct estimates of ocean heat transport, J. Climate, *2,* 1173–1184.

Krauß, W. 1986. The North Atlantic Current. J. Geophys. Res., *91,* (C4), 5061–5074.

Leaman, K. D., E. Johns and T. Rossby. 1989. The average distribution of volume transport and potential vorticity with temperature at three sections across the Gulf Stream, J. Phys. Oceanogr., *19,* 36–51.

Leaman, K. D. and J. E. Harris. 1990. On the average absolute transport of the Deep Western Boundary Currents east of Abaco Island, the Bahamas. J. Phys. Oceanogr., *20,* 467–475.

Lee, T. N., W. Johns, F. Schott and R. Zantopp. 1990. Western Boundary Current structure and variability east of Abaco, Bahamas at 26.5° N. J. Phys. Oceanogr., *20,* 446–466.

Levitus, S. 1982. Climatological atlas of the world ocean. NOAA Prof. Pap. 13, U.S. Govt. Print. Office, Washington, D.C.

—— 1984. Annual cycle of temperature and heat storage in the world ocean. J. Phys. Oceanogr., *14,* 727–746.

—— 1989. Interpentadal variability of temperature and salinity at intermediate depths of the North Atlantic Ocean, 1970–1974 versus 1955–1959. J. Geophys. Res., *94,* (C5), 6091–6131.

Lozier, M. Susan, M. S. McCartney and W. B. Owens. 1994. Anomalous anomalies in averaged hydrographic data. J. Phys. Oceanogr., *24,* 2624–2638.

Marotzke, J. and C. Wunsch. 1993. Finding the steady state of a general circulation model through data assimilation: application to the North Atlantic Ocean. J. Geophys. Res.,*98,* (C11), 20149–20167.

McCartney, M. S. 1992. Recirculating components of the deep boundary current of the northern North Atlantic, Prog. Oceanogr., *29,* 283–383.

Olbers, D. J., M. Wenzel and J. Willebrand. 1985. The inference of North Atlantic circulation patterns from climatological hydrographic data, Rev. Geophys., *23,* 313–356.

Redi, M. H. 1982. Oceanic isopycnal mixing by coordinate rotation. J. Phys. Oceanogr., *12,* 1154–1158.

Rhein, M. 1994. The Deep Western Boundary Current: tracers and velocities. Deep-Sea Res., *41,* 263–281.

Rhein, M., L. Stramma and U. Send. 1995. The Atlantic Deep Western Boundary Current: water masses and transports near the equator. J. Geophys. Res., *100,* (C2), 2447–2457.

Rintoul, S. R. 1991. South Atlantic interbasin exchange. J. Geophys. Res., *96,* (C2), 2675–2692.

Sarmiento, J. L. 1986. On the North and Tropical Atlantic heat balance. J. Geophys. Res., *91,* (C10), 11677–11689.

Sarmiento, J. L. and K. Bryan. 1982. An ocean transport model for the North Atlantic. J. Geophys. Res., *87,* (C1), 394–408.

Schiller, A. 1993. Assimilation hydrographischer Daten in ein Zirkulationsmodell des Atlantiks auf der Grundlage des adjungierten Verfahrens, Berichte aus dem Institut für Meereskunde an der Christian-Albrechts-Universität Kiel, No. 235, PhD thesis, 157 pp.

Schiller, A. and J. Willebrand. 1995. A technique for the determination of surface heat and freshwater fluxes from hydrographic observations, using an approximation adjoint ocean

circulation model, J. Mar. Res., 53, 433–451.

Schlitzer, R. 1993. Determining the mean, large–scale circulation of the Atlantic with the adjoint method, J. Phys. Oceanogr., 23, 1935–1952.

Schmitt, R. W., P. S. Bogden and C. E. Dorman. 1989. Evaporation minus precipitation and density fluxes for the North Atlantic. J. Phys. Oceanogr., 19, 1208–1221.

Smethie, W. M. and J. H. Swift. 1989. The Tritium:Krypton-85 Age of Denmark Strait Overflow Water and Gibbs Fracture Zone Water just south of Denmark Strait. J. Geophys. Res., 94, (C6), 8265–8275.

Treguier, A. M. 1992. Kinetic energy analysis of an eddy resolving, primitive equation model of the North Atlantic. J. Geophys. Res., 97, (C1), 687–701.

Trenberth, K. E., J. G. Olsen and W. G. Large. 1989. A global ocean wind stress climatology based on ECMWF analyses, NCAR Technical Note 338+STR, NCAR Boulder, Colorado.

Tziperman, E. and W. C. Thacker. 1989. An optimal-control/adjoint-equations approach to studying the oceanic general circulation. J. Phys. Oceanogr., 19, 1471–1485.

Tziperman, E., W. C. Thacker, R. B. Long, S. M. Hwang and S. R. Rintoul. 1992. Oceanic data analysis using a general circulation model. Part II: a North Atlantic model. J. Phys. Oceanogr., 22, 1458–1485.

Wijffels, S. E., R. W. Schmitt, H. L. Bryden and A. Stigebrandt. 1992. Transport of freshwater by the oceans. J. Phys. Oceanogr., 22, 155–162.

Woodruff, S. C., R. J. Slutz, R. L. Jenne and P. M. Steurer. 1987. A comprehensive ocean-atmosphere data set. Bull. Am. Soc., 68, 1239–1250.

Wunsch, C. 1978. The North Atlantic general circulation west of 50W determined by inverse methods. Rev. Geophys. Space Phys. 16, 583–620.